AIAA 2002-0140
Receptivity to Freestream Disturbances of Mach 4.5 Flow over A Flat Plate

Yanbao Ma and Xiaolin Zhong
University of California, Los Angeles

40th Aerospace Sciences Meeting & Exhibit
January 14–17, 2002 / Reno, NV

Receptivity to Freestream Disturbances of Mach 4.5 Flow over A Flat Plate

Yanbao Ma* and Xiaolin Zhong†

University of California, Los Angeles, CA 90095

1 Abstract

The mechanisms of the receptivity to freestream disturbances of a Mach 4.5 flow over a flat plate are studied by using both direct numerical simulations (DNS) and linear stability theory (LST). A high-order shock fitting scheme is used in the numerical simulations in order to account for the effects of interactions between freestream disturbance waves and shock wave. The results show that the receptivity of the flat plate boundary layer to freestream fast acoustic waves leads to the excitation of both Mack modes and a family of linearly stable modes, i.e., mode I, mode II, etc. These modes play a very important role in the receptivity process of excitation of the unstable Mack modes, especially the second mode. Though mode I and mode II waves are linearly stable, they can have resonant (synchronization) interactions with both acoustic waves and the Mack-mode waves. The stable wave modes such as mode I and mode II are critical in transferring wave energy between the acoustic waves and the unsteady second mode. The receptivity of the unstable second Mack-mode waves to freestream fast acoustic waves is mainly through their resonant interactions with mode I waves. The receptivity mechanisms for flow over a flat plat at Mach 4.5 to freestream acoustic waves has been studied. The effects from frequencies, incident wave angles, and wall boundary conditions on the boundary-layer stability and receptivity are studied.

2 Introduction

The study of laminar-turbulent transition in supersonic and hypersonic boundary layers is important to the development of future space vehicles operating at sustained supersonic and hypersonic speeds. In an environment with small initial disturbances, the paths to transition can conceptually be divided into three stages: 1) receptivity, 2) linear eigenmode growth or transient growth, and 3) nonlinear breakdown to turbulence. The first stage is the receptivity process, which converts the environmental disturbances into instability waves, such as the Tollmien-Schlichting (T-S) waves, in the boundary layers. The study of the receptivity mechanisms is important because it provides important initial conditions of amplitude, frequency, and phase angles for the instability waves in the boundary layers [1]. The main objective of a receptivity study of a boundary layer is to investigate the properties and mechanisms of initial generation of unstable boundary-layer wave modes by forcing waves.

This paper is concerned with the receptivity of a supersonic boundary layer over a flat plate. The unstable wave modes in a supersonic boundary layer have been identified and extensively studied by Mack [2] using the LST. Mack found that, in a supersonic boundary layer of relatively high Mach numbers, there are multiple higher instability modes in addition to the first instability mode, which is the compressible counterpart of T-S waves in incompressible boundary layers. Among them, the second mode is most interesting because it becomes the dominant instability in supersonic boundary layers at Mach numbers larger than about 4. On the other hand, the oblique first mode is most unstable for supersonic flow at lower Mach numbers. Therefore, the receptivities of the first and the second modes to forcing disturbances are the main goal of a receptivity study.

Though the linear stability properties of the unstable Mack modes in supersonic boundary layers are well understood, it is still a subject of current research with regard to the receptivity of the supersonic boundary layer, i.e., the generation mechanisms of the unstable Mack modes by various forcing waves. There have been a number of experimental studies on the receptivity of supersonic and hypersonic boundary layers [3–5]. It was found that the forcing fast acoustic waves impinging on the leading edge generate Tollmien-Schlichting waves in supersonic boundary layers. There is a dependence of receptivity coefficients on the incident wave angles of the forcing waves. On the other hand, most of the computational and theoretical studies on boundary-layer receptivity have been mostly for incompressible flow [1]

*Graduate Student Researcher, Department of Mechanical and Aerospace Engineering

†Associate Professor, Department of Mechanical and Aerospace Engineering, Associate Fellow AIAA.

There have been only a few theoretical and computational studies on the receptivity of compressible boundary layers [6–9]. Recently, Fedorov *et al.* [10,11] did analytical analyses to show that strong excitation occurs when external waves and wall induced disturbances are in resonance with the boundary-layer normal modes. Boundary-layer self-similar solutions were used in Fedorov's analyses. The effect of the bow shock wave on the receptivity process, however, was not considered. Zhong [12,13] studied the receptivity of hypersonic flow over a parabola by numerical simulations of the full Navier-Stokes equations. The effects of bow shock interactions and the entropy layer are accurately taken into account by using a fifth-order shock-fitting scheme. It was concluded that the generation of boundary-layer stability waves was mainly due to the interaction of boundary layer with the transmitted fast acoustic waves instead of entropy and vorticity waves. The receptivity coefficient was found to increase as the relative nose radius was decreased. Malik *et al.* [14] studied the receptivity of Mach 8 flow past a sharp wedge with 5.3° half angle to three different types of external disturbances by solving compressible linearized Navier-Stokes equations. The forcing disturbances include a surface suction/blowing embedded in wedge surface, a narrow beam of freestream fast acoustic waves, and plane freestream fast acoustic waves in the freestream. Their results showed that similar boundary-layer instability wave patterns are resulted in all cases of different forcing freestream disturbance waves. No qnantitative analysis of the supersonic boundary-layer receptivity mechanism was done on the computational results.

Figure 1 shows a schematic of the receptivity process of a supersonic flat-plate boundary layer to freestream disturbances. An oblique bow shock wave is generated in supersonic viscous flow over a flat plate due to the displacement of the boundary layer by the viscous effects. The strength of the bow shock, which is not known in advance, depends on the freestream Mach number and Reynolds number of the flow. The induced oblique shocks were neglected in most of the previous theoretical and computational studies of the stability and receptivity of supersonic and hypersonic boundary layers. Such simplification is acceptable in the LST [2]. because the standoff distance of the shock away from the wall is relatively large compared with the boundary-layer thickness. For the study of the supersonic boundary-layer receptivity to freestream disturbances, however, the effects of the oblique shock on the receptivity can be significant, hence cannot be neglected. In the receptivity process, the forcing freestream disturbance waves need to pass through the oblique shock wave before they enter the boundary layer to excite the unstable Mack modes. The interactions between the shock wave and the forcing waves generate complex wave patterns behind the shock. Therefore, it is necessary to include the shock interaction in numerical simulation studies of supersonic boundary-layer receptivity.

The objective of this paper is to study the receptivity mechanisms of the supersonic boundary layer to freestream acoustic waves by numerical simulations. In the simulation, the freestream acoustic waves are superimposed on the steady base flow to investigate the generation and development of boundary-layer instability waves. A plane freestream fast acoustic wave at $F = 2.2\times10^{-4}$ with zero angle ($\theta_{ac} = 0$) was studied in our previous paper [15]. However, different components of discrete wave modes involved in boundary-layer disturbances was not completely identified. Therefore, the same case are studied in this paper in order to completely identify all different wave modes induced in boundary-layer disturbances by forcing freestream fast acoustic waves. The receptivity properties are analyzed based on numerical simulations and by the LST analyses. The effects of forcing incident wave angles, forcing wave frequencies, and wall temperature perturbations on the receptivity are studied in this paper.

3 Governing Equations and Numerical Methods

The governing equations, the numerical methods, and the flow parameters are briefly described in this section. Under thermally and calorically perfect gas regime, the two-dimensional Navier-Stokes equations in conservative form can be written as:

$$\frac{\partial \mathbf{U}^*}{\partial t^*} + \frac{\partial}{\partial x^*}(\mathbf{F}_1^* + \mathbf{F}_{\mathbf{v1}}^*) + \frac{\partial}{\partial y^*}(\mathbf{F}_2^* + \mathbf{F}_{\mathbf{v2}}^*) = 0\,, \quad (1)$$

where the superscript "$*$" represents dimensional variables, and $\mathbf{U}^*$ is a vector containing the conservative variables, $\{\rho^*, \rho^* u^*, \rho^* v^*, e^*\}$. $\mathbf{F}_1^*$ and $\mathbf{F}_2^*$ are inviscid flux vectors, and $\mathbf{F}_{\mathbf{v1}}^*$ and $\mathbf{F}_{\mathbf{v2}}^*$ are viscous and diffusive flux vectors. In the numerical simulations, a constant Prandtl number of $Pr = 0.72$ is used, and the viscosity coefficient are calculated by using the Sutherland's law.

In this paper, dimensional flow variables are nondimensionalized using the steady-state freestream conditions. Specifically, velocities are nondimensionalized by the freestream velocity U_∞^*, length scales by a boundary-layer thickness length L^* given by Eq. (4), density by ρ_∞^*, pressure by p_∞^*, temperature by T_∞^*, time by L^*/U_∞^*, vorticity by U_∞^*/L^*, entropy by c_p^*,

wave number by $1/L^*$, circular frequency by u^*_∞/L^*, etc. The dimensionless flow variables are denoted by the same notations as their dimensional counterparts but without the superscript.

A fifth-order shock-fitting method of Zhong [16] is used to compute the two-dimensional Navier-Stokes equations in the flow field bounded by the bow shock and the plate (Figure 1). The shock-fitting method treats the bow shock as a computational boundary. The flow variables behind the shock are determined by Rankine-Hugoniot relations across the shock and a characteristic compatibility equation from behind the shock. The transient movement of the shock and its interaction with freestream disturbance waves are solved as a part of the solutions. The use of shock-fitting method make it possible to use high-order finite difference scheme for spatial discretization. Fifth-order upwind finite difference scheme is applied for convective terms while sixth-order central scheme for the discretization of viscous terms. The spatial discretization of the governing equations leads to a system of first-order ordinary differential equations. Explicit Runge-Kutta method is used for temporal discretization. The detail numerical method has been presented in the previous paper [15]. They are not repeated here.

Non-slip wall boundary condition is used for velocity. Adiabatic wall boundary condition is used for the steady base flow. For unsteady flow simulations, the boundary conditions for temperature fluctuations at the wall satisfy either adiabatic wall ($\partial T'/\partial y = 0$) or isothermal wall ($T' = 0$) conditions. It has been argued [2,17] that it is more physical to assume that the temperature perturbations vanish at the solid boundary even though an adiabatic wall boundary condition is used to calculate the base flow. In reality, the temperature perturbations could be somewhere between zero perturbation for isothermal condition and zero normal gradient for adiabatic condition. Therefore, in this paper, both the adiabatic wall and isothermal wall boundary conditions are used for the temperature perturbations as two bounds for real cases if physical condition for temperature perturbations is difficult to determine. The effect of the two wall temperature boundary conditions on the boundary-layer instability wave growth rates will be investigated and discussed.

4 Flow Conditions

The receptivity of a Mach 4.5 boundary-layer flow over a flat plate is considered because the stability of this Mach 4.5 flow has been extensively studied [18–20]. The flow conditions are same as those used in Kendall's [21] experiment on the stability of a Mach 4.5 flow over a flat plate, i.e.,

$$M_\infty = 4.5\,, \qquad T^*_\infty = 65.15\,K\,,$$
$$p^*_\infty = 728.4381557Pa\,, \qquad Pr = 0.72\,,$$
$$Re^*_\infty = \frac{\rho^*_\infty U^*_\infty}{\mu^*_\infty} = 7.2\times 10^6 m^{-1}\,.$$

In many figures of this paper, the results are plotted as a function of dimensional x^* coordinate along the flat plate because this case has been studied by previous experiments. The dimensional x^* coordinate in the figures can be easily converted to dimensionless local Reynolds numbers according to the following formula:

$$Re_x = Re^*_\infty\, x^* = 7.2\times 10^6 x^*\,, \tag{2}$$

where x^* is the dimensional coordinate in meters measured from the leading edge along the plate surface for the current simulations.

The computational domain of the current simulations by using the shock-fitting method begins at $x^* = 0.006m$ and ends at $0.63m$, corresponding to the local Reynolds numbers ranging from $Re_x = 0.432\times 10^5$ to $Re_x = 4.54\times 10^6$. In studies of boundary-layer stability, the following Reynolds number, R, based on the length scale of boundary-layer thickness are often used:

$$R = \frac{\rho^*_\infty u^*_\infty L^*}{\mu^*_\infty}\,, \tag{3}$$

where length scale of boundary-layer thickness is defined in this paper as

$$L^* = \sqrt{\frac{\mu^*_\infty x^*}{\rho^*_\infty u^*_\infty}}\,. \tag{4}$$

Hence, the relation between R and local Reynolds number Re_x is

$$R = \sqrt{Re_x}\,. \tag{5}$$

In terms of R, the full computational domain of the current simulations spans from $R = 207.9$ to $R = 2129.8$. In the actual simulations, the computational domain is divided into 11 sub-zones with a total of 3121 grid points in the streamwise direction and 121 grid points in the wall-normal direction. From supersonic boundary-layer self-similarity solutions, the displacement thickness of the current boundary layer is approximately $12.9L^*$. Grid stretching function is used

in wall-normal direction to cluster more points inside the boundary layer near the wall. The grid points are distributed uniformly in the streamwise direction. The numerical accuracy of the results based on this grid assignment has been evaluated by grid refinement studies to ensure grid independence of the numerical solutions, which is shown in the previous paper (Ma & Zhong 2001).

5 Boundary-Layer Wave Mode Characteristics

The purpose of the boundary-layer receptivity study is to find out how environment disturbances enter the boundary layer and generate boundary-layer instability waves. The instability waves in supersonic boundary layers, such as the first and the second modes, have been studied extensively by Mack [2] and other researchers by using the approach of the LST. However, previous LST studies have been mainly focused on the instability of the first- and second-mode waves. In a receptivity process, it is found that some other wave modes, which are stable in a linear stability analysis, play an important role in the receptivity process. In order to understand the receptivity process, it is necessary to understand the characteristics of these stable wave modes. Therefore, as the first step in studying the receptivity of a supersonic boundary layer to freestream disturbances, the characteristics of normal modes of the Mach 4.5 boundary layer are studied by the LST in this section. A LST computer code based on multi-domain spectral method of Malik [17] is developed to carry out the LST to identify instability modes.

Modes I, II, III and IV

The characteristics of Mach 4.5 ($Re^*_\infty = 7.2\times10^6/m$) boundary-layer normal modes are studied. The base flow obtained from self-similar boundary-layer solutions are used to perform the LST because it is easier to obtain self-similar base flow solutions at arbitrary locations. Our calculations have shown that the linear stability properties based on steady flow solutions from numerical simulations are very close to those based on self-similar steady boundary-layer solutions. Therefore, the self-similar base flow solutions are used in the LST calculations in this section in order to extend the stability calculation to much further downstream.

In the first test case, the eigenvalues α associated with different modes are identified and tracked from upstream to downstream with fixed frequency $F = 2.2 \times 10^{-4}$ (spanwise wave number $\beta = 0$ for two-dimensional waves). Here, adiabatic boundary condition for temperature disturbances is used. After complex parameter α is found, a non-dimensional phase velocity of the normal mode can be calculated as

$$a = \frac{RF}{\alpha_r}. \tag{6}$$

Either phase velocity a or the real part of the wave number α_r can be used to characterize the normal mode inside the boundary layer. Figure 2 shows the distributions of the phase velocities of boundary-layer wave modes. The phase velocity distributions shown in this figure include the following two computational cases:

- Case 1: phase velocity distributions as a function of different streamwise locations R at a fixed frequency of $F = 2.2 \times 10^{-4}$.
- Case 2: phase velocity distributions as a function of different frequencies F at a fixed streamwise location of $R = 2000$.

The figure shows that the two cases have identical phase velocity curves when they are plotted as functions of $\omega = RF$. In general, the phase velocities of different normal modes inside the boundary layer can be written as a function of nondimensional circular frequency ω for cases of different frequencies F and different local Reynolds numbers R.

This figure shows the phase velocities of the first several wave modes in the supersonic boundary layer. The phase velocities of the fast acoustic wave $(1 + 1/M_\infty)$, entropy/vorticity wave (1), and slow acoustic wave $(1-1/M_\infty)$ are also shown in the figure for comparison. In the figure, there are a class of wave modes, which are originated with a initial phase velocity of the fast acoustic wave $(1+1/M_\infty)$. Before these wave modes become distinct modes, their eiguvalues merge with the continuous spectra. After these wave modes appear, their phase velocities decrease gradually as they propagate to downstream. In this paper, we define these wave modes as mode I, mode II, mode III, etc. according to the sequences of their appearance. Specifically, mode I appears from the leading edge; mode II comes out next, followed by mode III, and so on. In further downstream, even higher modes will appear.

Figure 3 shows the typical eigenfunction profiles of this class of modes at $R = 4000$ and $F = 2.2 \times 10^{-4}$. At this location, there is only one peak for mode I disturbances, while there are one peak and one valley for mode II, two peaks and one valley for mode III , two peaks and two valleys for mode IV disturbances. This

figure also shows that the disturbances of this family of modes are mainly concentrated inside the boundary layer (the boundary-layer displacement thickness is about $\delta^* = 12.9L^*$). When this class of disturbances propagate from upstream to downstream, the total number of peaks and valleys for pressure disturbance profiles does not change, although the locations of peaks and valleys can change gradually.

Mack modes (1st, 2nd, and 3rd modes)

Besides the family of wave modes I, II, III defined above, Fig. 2 shows that there is another wave mode starting from the leading edge with an initial phase velocity close to $1 - 1/M_\infty$ near the leading edge. For this mode, its phase velocity is less than the freestream velocity, and approaches the value of the freestream velocity as it propagates to downstream. This mode is termed the Mack modes because different sections of this mode shown in the figure have been defined by Mack [2] as the first, second, and third modes as marked in the figure. It should be pointed out that the first, second, third modes defined by Mack are in fact different section of a single Mack mode as shown in Fig. 2.

In the phase velocity curves shown in Fig. 2, the Mack modes intersect with Mode I, II, III, and IV subsequently as RF increases. At the intersections of the phase velocity curves, the Mack modes are synchronized with mode I, mode II, mode III, or higher modes because they have the same frequency and phase velocity there. The synchronization of two wave modes can lead to resonant interactions between the two waves. Unlike mode I, II and III, whose numbers of the peaks and valleys do not change as R increase for a fixed F, the total number of peaks and valleys for pressure disturbance profiles of the Mack modes increase gradually when the Mack mode waves propagate from upstream to downstream. For example, near the leading edge, there is only one peak for pressure disturbance profile of the Mack mode. After the synchronization with mode I, another valley appears in pressure disturbance profile. Mack defined the numbering of these modes as first mode with one peak in pressure profile, second mode with one peak and one valley, etc.

When the first mode propagates to downstream, it is synchronized with mode I when the two modes intersect in the phase velocity curves. At the location of synchronization ($R = 845$ for $F = 2.2 \times 10^{-4}$), both the first mode and mode I have almost the same profiles of disturbances inside the boundary layer, which is shown in Fig. 4. As a result, it is almost impossible to distinguish mode I from the first mode based on the profiles of disturbances at this location. Because both the first mode and mode I have the same phase velocity at their synchronization location, it is impossible to identify them from the phase velocity either. The characteristic that can distinguish them is the change of phase velocities during propagation. The phase velocity of mode I decreases while that of the first mode increases during their propagation to downstream. After the synchronization point between mode I and the first mode, another valley gradually appears in the profile of pressure disturbances for the Mack mode. The Mack mode in this region is called the second mode. When the second mode propagates to downstream, it gets synchronized with mode II. At the location of synchronization ($R = 2509$ for $F = 2.2 \times 10^{-4}$), both the second mode and mode II have almost the same profiles of disturbances inside the boundary layer, which is shown in Fig. 4. This figure also shows that there is much stronger oscillation in the profiles of the second mode disturbances near the edge of the boundary layer ($\delta^* = 12.9L^*$) compared with that of mode II. At the location of Mack-mode synchronization with mode II, another peak appears in the profile of pressure disturbances for the Mack mode, which is the characteristic of the third mode based on Mack's definition. Actually, the profiles of Mack mode at $R = 2509$ shown in Fig. 4 are located in the transition region from the second mode to the third mode. Similarly, the Mack mode will get synchronized with mode III and become the fourth mode when it propagates to further downstream (Fig. 2).

Stability of boundary-layer normal modes

The phase velocity distributions of disturbances combined with growth rates (α_i) and disturbance profiles are important parameters to identify different normal modes. The growth rates of different normal modes for the previous two groups of computational cases are plotted in Fig. 5. In this figure, different symbols stand for the first group of cases of different R at a fixed frequency of $F = 2.2 \times 10^{-4}$, and line patterns represent the second group of cases of different F at a fixed Reynolds number of $R = 2000$. For both groups of cases, the growth rates for mode I, II, III and IV are always positive, which means this family of modes are always stable. Furthermore, the values of α_i of these modes increase as they propagate to downstream, which indicates that these modes become more and more stable during their propagation to downstream. Figure 5 also shows that only the Mack modes are unstable in the range of $R * F$ between 0.18 and 0.23, in which the unstable Mack modes are the conventional second mode. In this range, the growth rates of the second mode change dramatically. As shown in the figure, the slope of the growth rate curve for the second mode is very sharp in this range. The shape of

growth rate curve of the unstable second mode is almost the same for the two groups of cases of fixed frequency at $F = 2.2 \times 10^{-4}$ and fixed Reynolds number at $R = 2000$. In addition, the locations of the branch I and II neutral stability points of the second mode in terms of $R * F$ are almost same for both group of computational cases.

Effect of temperature boundary condition

To study the effect of wall boundary condition for temperature perturbations on the stability characteristics of the boundary-layer normal modes, eigenvalues associated with different modes at fixed location ($R = 2000$) are obtained for a range of frequencies with both isothermal and adiabatic wall boundary conditions. The results of the isothermal case are compared with those of the adiabatic case. Figure 6 and 7 compares the phase velocities and the growth rates of the relevant normal modes as a function of ω ($\omega = R * F$). Different line patterns show the phase velocities of different normal modes for the isothermal case while different symbols denote those for the adiabatic case. The figure shows that the phase velocities of normal modes are the same for both isothermal case and adiabatic case, which shows that the effect of wall temperature disturbance boundary condition on the phase velocities is very small. This figure also shows that all normal modes of the isothermal case are more stable than the corresponding modes of the adiabatic case.

6 Forcing Waves from Inlet

The characteristics of unsteady Mack modes have been studied by both DNS and LST in our previous paper [15]. The characteristics of steady boundary-layer modes, mode I and mode II, are studied by numerical simulations in this section. Mode I and mode II waves with fixed frequency are imposed at the inlet to study the wave modes characteristics and resonant interactions in the supersonic boundary layer. The profiles of the forcing waves at the inlet are specified as those obtained from the LST. At the inlet boundary of the computational domain, the flow is specified as the superposition of the steady base flow and a temporal fluctuations of flow variables at frequency ω, amplitude ϵ, and streamwise wave number α_r, i.e,

$$\phi(x_{in}, y, t) = \bar{\phi}(x_{in}, y) + \epsilon\hat{\phi}(y)e^{i(\alpha_r x_{in} - \omega t)} \qquad (7)$$

where $\phi(x_{in}, y, t)$ represents any of the flow variables. For a given wave mode at a fixed frequency, the wave number α_r and the disturbance structure contained in $\hat{\phi}(y)$ is obtained from the LST results. Because x_{in} is fixed at the inflow, the product of $\alpha_r x_{in}$ is a constant for a given α_r. This constant can only affect the phase angle at the inflow. Therefore, it is not necessary to specify α_r when a normal mode is introduced at the inlet. The subsequent downstream propagation of this wave mode and its interactions with other modes are simulated by time-accurate computations of the full Navier-Stokes equations.

6.1 Mack modes at different frequencies

The effects of wave frequency on the propagation of the Mack modes are studied by comparing the results of four cases with different frequencies, i.e.

$$F = 0.6 \times 10^{-4}, 1.2 \times 10^{-4}, 1.6 \times 10^{-4}, 2.2 \times 10^{-4}.$$

The adiabatic boundary condition is used for the temperature perturbations on the wall for these computational cases. Figure 8 compares amplitudes of pressure perturbations on the wall for the four cases with different frequencies when the Mack-mode waves with the same initial pressure amplitude of $|p'|/p_\infty = 0.0002835$ are imposed at the inlet. The inlet of the four cases has the same location of $x^* = 0.025m$ ($R = 424.26$), where the Mack mode is in the first mode region. The figure shows that as the frequencies decrease, the growth rates of the Mack mode increase and the locations of branch II neutral stability points move downstream.

The effects of frequencies on the growth rates and the locations of branch II neutral stability points are consistent with the LST prediction. Based on the LST prediction, the locations of branch II neutral stability point of the second mode in terms of $R * F$ are same for cases of different frequencies (Figs. 5). The peak amplitude of pressure perturbations at the branch II neutral stability point for the case of $F = 2.2 \times 10^{-4}$ is located at $x^* = 0.155m$, or $R * F = 0.2324$ ($R = 1056$). Therefore, it is expected that the peak amplitudes of pressure perturbations for cases of $F = 1.6 \times 10^{-4}$ and $F = 1.2 \times 10^{-4}$ should be located at $R * F = 0.2324$ also, i.e., $R = 1452.6$, or $x^* = 0.293m$ for the case of $F = 1.6 \times 10^{-4}$, and $R = 1936.7$ or $x^* = 0.521m$ for the case of $F = 1.2 \times 10^{-4}$. From the numerical simulation with $F = 1.6 \times 10^{-4}$, the peak amplitude of pressure perturbation is $|p'|/p_\infty = 0.003774$ and located at $x^* = 0.2914m$ ($R = 1448.5$). For the case of $F = 1.2 \times 10^{-4}$, the peak amplitude of pressure perturbation is $|p'|/p_\infty = 0.007658$ and it is located at $x^* = 0.5188m$ ($R = 1932.7$). Therefore, the locations of the peak pressure amplitudes from the numerical simulations are consistent with those predicted by the LST.

On the other hand, the peak value of pressure perturbations for the case of $F = 1.2 \times 10^{-4}$ is almost quadruple of that for the case of $F = 2.2 \times 10^{-4}$ and twice of that for the case of $F = 1.6 \times 10^{-4}$. This can be explained from the LST prediction on the growth rates of the second mode. For different frequencies, there are very similar growth rate curves in the second-mode unstable region in terms of $R * F$ shown in Fig. 5. $R * F$ is proportional to the square root of physical length x^* for a fixed frequency. For different frequencies, the second-mode unstable region expressed in x^* should be longer for lower frequency case given the same range of $R * F$. From the definition of growth rates [15], the amplitude changing with x can be obtained by taking integration of growth rates with respect to x^* according to the following formula:

$$|\phi'|(x^*) = |\phi'_0| e^{\int_{x_0^*}^{x^*} -\alpha_i(\omega) dx^*}, \tag{8}$$

where $|\phi'_0|$ is the initial wave amplitude at x_0^*. Therefore, a longer integration range in the second-mode unstable region leads to larger disturbance amplitudes for the cases of lower frequency given the same initial wave amplitudes.

For the case with $F = 0.6 \times 10^{-4}$, the unstable region of the second mode is out of the range of the current computational domain ($0.02592 < R * F < 0.128$), while the first mode is slightly unstable from the LST prediction. The LST prediction agrees with the simulation results as shown in Fig. 8. The first-mode branch II neutral stability point from the LST is located at $x^* = 0.536$ ($R = 1963.6$). From simulation, pressure perturbation reach peak value of $p'/p_\infty = 0.001226$ at $x^* = 0.573$ ($R = 2031.16$). The numerical solutions agree well with those of the LST prediction in term of the location of the branch II neutral stability point for the first mode.

Figure 9 compares the growth rates as a function of $R * F$ between the results from LST and numerical simulations for two cases of different frequencies, i.e., $F = 2.2 \times 10^{-4}$ and 1.6×10^{-4}. Again, the growth rate curves obtained from the numerical simulations for two cases of different frequencies are very close to each other, except that the peak growth rate is slightly larger for the case of $F = 1.6 \times 10^{-4}$. The locations of the peaks at different frequencies are approximately the same. Therefore, both the results from the LST predictions (Figs. 5) and those from numerical simulations (Fig. 9) show that the growth rate curves of the second mode *vs.* $R * F$ are very close for different frequencies. As discussed before, compared with the numerical solutions, the corresponding LST results under predict the growth rates of the second mode in the supersonic boundary layer.

Therefore, the results predicted by the LST are accurate in predicting the wave numbers and wave mode structures of the Mack modes in the supersonic boundary layer, but the LST results are not accurate in predicting the growth rates of the Mack modes. The LST calculations consistently under predict the growth rates as compared with the full Navier-Stokes simulations.

6.2 Mode I Propagation and Resonant Interactions with Mack Modes

Mode I at $F = 2.2 \times 10^{-4}$

The development of mode I waves in the boundary layer is considered in this section, where forcing disturbances of mode I with a frequency of $F = 2.2 \times 10^{-4}$ are introduced at the inlet of the computational domain located at $x^* = 0.025m$ ($R = 424.26$). Though this mode is always stable according to the LST prediction, it is important to the supersonic boundary-layer receptivity process. Unlike the Mack mode with a single mode propagation without significant excitation of other modes, the simulation results in this section show that mode I can convert to the Mack-mode waves in the boundary layer through the resonant interactions between mode I and the Mack modes. Such resonant interactions are the key to the receptivity of the second mode in the supersonic boundary layer.

Figure 10 shows the instantaneous pressure disturbances along the wall surface after the unsteady solutions reach a periodic state. There are multiple peaks in amplitudes in pressure perturbations, which indicates the excitation of different wave modes at different locations of the wave propagation from the inlet to downstream. The amplitudes of pressure disturbances increases before reaching the first peak located approximately at $x^* = 0.06m$, which means this mode is unstable in this region. This is contradictory to the LST prediction shown in Fig. 5 that mode I should be always stable. Intuitively, the amplification of mode I may due to effect of the shock wave, which is not included in the LST. A similar numerical simulation on the propagation of mode I is performed by using a rectangle domain without the shock wave and boundary-layer self-similar solutions are used as inflow conditions (Ma & Zhong 2000). Figure 11 compares the amplitudes of pressure perturbations for two simulations with and without shock. This figure indicates that the effect of the shock on the propagation of mode I disturbances in the boundary layer are negligible. One possible reason for the amplification of mode I is resulted from

the interaction between mode I disturbances and other discrete modes or continuous disturbances in the flow field.

After passing the first peak (at $x^* = 0.06m$), mode I waves decay due to its inherent stable property. Figure 10 show a second growth region for mode I in the range of x^* between $0.115m$ to $0.155m$. This growth results from resonant interaction between mode I and the first mode when the two modes intersect at the synchronization point shown in Fig. 2. As shown in Fig. 4, both the first mode and mode I have almost the same profiles of disturbances across the boundary layer at the synchronization point. As a result, mode I waves convert to the Mack-mode waves in the synchronization region. After the synchronization point between mode I and the first mode, the Mack mode becomes the second mode, which is unstable in the region closely behind the synchronization point. The wave amplitudes in the region after the synchronization point increase because of the growth of the induced second mode in its unstable region. Therefore, the boundary-layer disturbances obtained by the numerical simulation are amplified again when they reach the second-mode unstable region because the second mode are induced by resonant interaction with mode I.

The process that mode I waves convert to the second mode waves is also shown in the distribution of the phase velocities calculated from the numerical solutions of the pressure disturbances along the wall surface as shown in Fig. 12. The figure shows that the phase velocities obtained from the simulation are the same as those of mode I predicted by the LST in the upstream region. This is expected because the disturbances imposed at the inlet are those of mode I obtained from the linear stability analysis. As the wave propagates downstream, mode I has an energy exchange with the second mode at the wave synchronization point between mode I and the Mack mode located approximately at $x^* = 0.1m$. The Mack mode is excited by the interaction with mode I at the synchronization point. After the synchronization point, the second mode induced by mode I propagates downstream. The amplitudes of the second Mack mode grow in the subsequent unstable region until it reaches branch II neutral stability point. After the Mack-mode waves pass branch II neutral stability point of the second mode, the amplitudes of disturbances decay rapidly in the second-mode stable region. There are strong oscillations in the phase velocity distribution after the decay of the second mode because the disturbances result from the modulation of the second mode and mode II excited further downstream. Finally, both mode II and the Mack-mode disturbances die down in the downstream.

These results indicate that although mode I is always stable, it can play an important role in the receptivity process because it can convert to the unstable Mack mode through the resonant interaction with Mack modes. The amplitudes of the induced Mack mode can grow in its unstable region immediately following the wave synchronization point.

Effect of wall temperature boundary conditions

The effect of the wall temperature boundary conditions on the propagation of mode I is investigated by introducing mode I disturbances at the inlet with both the isothermal wall and the adiabatic wall boundary conditions. The inlet is located at $x^* = 0.025m$ ($R = 424.26$), and the initial pressure amplitude is $|p'|/p_\infty = 0.0002835$. Two cases with different frequencies of $F = 2.2 \times 10^{-4}$ and $F = 1.2 \times 10^{-4}$ are studied. Figure 14 compares the amplitudes of pressure perturbations on the wall between the cases with two different wall temperature boundary conditions and two different frequencies. Overall, the amplitudes of pressure perturbations away from the inlet are much smaller for the isothermal cases compared to those of the adiabatic cases with the same frequency. Especially, at the same frequency, pressure amplitudes at the second-mode branch II neutral stability points are much smaller in the isothermal case than those in the adiabatic case. The reason for the difference in wave amplitudes between the adiabatic cases and the isothermal cases is that the normal modes of the isothermal cases are linearly more stable than those of the adiabatic cases (Fig. 7). Compared with an adiabatic case, mode I in an isothermal case is less amplified before it reaches the first peak in pressure perturbations. Furthermore, the amplitudes of mode I disturbances in the isothermal case decay much faster and die down to a much smaller value when the wave reaches the synchronization point between mode I and the Mack modes. As a result, the initial amplitudes of the induced second-mode waves are much smaller in the isothermal cases than those in the corresponding adiabatic cases. In addition, the growth rates of the second mode shown in Fig. 7 are smaller for the isothermal case than those for the adiabatic case. Therefore, the amplitudes of induced second-mode waves at branch II neutral stability point are significantly smaller for the isothermal cases than those for the adiabatic cases.

6.3 Mode II Propagation and Resonant Interactions with Acoustic Waves

The development of mode II waves in the boundary layer is considered in this section. Similar to mode

I, this mode is always stable according to the LST prediction, but they are important to the supersonic boundary-layer receptivity process. As shown in Fig. 2, mode II was initiated at the same phase velocity as that of the freestream fast acoustic wave at $1+1/M_\infty$. As mode II propagates downstream, its phase velocity decreases. Mode II can have a energy exchange with the fast acoustic waves in the boundary layer through these resonant interactions. Such resonant interactions are critical to the receptivity of the Mack mode in the supersonic boundary layer.

The results of two test cases of mode II propagation are presented in this section. In these cases, mode II disturbances of the same frequency are imposed at different inlet locations. In the first case, the initial mode II waves are imposed at $RF = 0.3552$. Figure 2 shows that the inlet location of this case is in the downstream of the location where mode II first appear in Fig. 2. On the other hand, in the second case, the initial mode II waves are imposed at $RF = 0.2539$. The inlet location is near the location of first appearance of mode II. The results in this case will show that the subsequent development of mode II is very different in these two cases because there are wave interaction near this synchronization point between mode II and the fast acoustic waves.

Mode II imposed at the inlet with $RF = 0.3552$

In this case, the forcing disturbances of mode II with a frequency of $F = 2.2 \times 10^{-4}$ are introduced at the inlet of the computational domain located at $x^* = 0.362m$ ($R = 1614.43$). The adiabatic wall boundary condition is used for the temperature perturbations on the wall. The inlet is located at $RF = 0.3552$ in the phase velocity plots of Fig. 2, which shows that mode II is imposed from downstream of its initial synchronization point with the fast acoustic wave.

Figure 15 shows the contours of instantaneous density perturbations obtained from the numerical simulation after the flow solution reaches a periodic state. Unlike the density contours of the second mode, the density disturbances of mode II do not have the rope-like density wave patterns, which is a signature mark of the second mode. Figure 16 shows the instantaneous pressure disturbances along the wall surface. The decaying of pressure disturbances indicates that mode II waves are stable, which is consistent with the prediction of the LST (Fig. 5). This figure show the simulation results of this case only contains the disturbances of pure mode II waves in the boundary layer. No other wave modes are excited. As predicted by the linear stability analysis, the wave mode is stable as it propagates downstream. The results of numerical simulations are expected to agree with the LST results because there is no other wave components in the solutions.

Figure 17 compares the profiles of disturbances at $x^* = 0.488m$ ($R = 1874.46$) obtained from the numerical simulation and those predicted by the LST as the eigenfunctions of mode II. The figure shows an excellent agreement in the disturbance structures between the numerical results and the LST predictions. Figure 18 shows the comparison of streamwise wave numbers (α_r) and growth rates (α_i) obtained by the numerical simulation and the corresponding values predicted by the LST. The figure shows a very good agreement in streamwise wave numbers. Therefore, there are only pure mode II waves in the boundary layer. The eigenfunctions and wave numbers of the waves can be predicted very well by the linear stability analysis. However, consistent with other modes, the LST analysis overpredicts the growth rates (α_i) of mode II in the boundary layer as shown in Fig. 19. Therefore, there are significant differences on the growth rates between the LST predictions and the numerical simulation results (larger than 50% in maximum). Again, the differences may be due to the fact that a parallel assumption is used in the linear stability analysis, while the actual boundary layer is not parallel. The nonparallel effect becomes stronger at higher Mach numbers.

Mode II imposed at inlet with $RF = 0.2539$

In this case, mode II disturbances at a fixed frequency $F = 2.2 \times 10^{-4}$ are introduced through the inlet at $x^* = 0.185m$ ($R = 1154.12$). This case is different from the previous case only in the location of the inlet. For previous case, the inlet is located in the downstream of the initial synchronization point between mode II waves and fast acoustic waves. For this case, the inlet is located at $R = 1154.12$ ($RF = 0.2539$), which is very close to the synchronization point between mode II waves and fast acoustic waves. The profiles of mode II disturbances at the inlet are showed in Fig. 20. It shows that the wave structures of mode II at this early location contain strong amplitudes in region outside the boundary layer.

Figure 21 shows the contours of instantaneous density perturbations obtained from the numerical simulation after the flow field reaches a periodic state. The results show a strong wave field outside the boundary layer near the inlet location. Compared with the previous case of a single mode II wave propagation in the boundary layer, the wave field in the current case is much more complex because of the wave-mode synchronization between mode II and the fast acoustic wave at the inlet. Figure 22 shows the distribution of instantaneous pressure disturbances along the wall

surface. Compared with the previous case of mode II propagation shown in Fig. 16, Fig. 22 shows that the disturbance field of the current case contains a mixture of several wave modes with multiple peaks in perturbation amplitudes. Even though mode II is always a stable mode according to the LST analysis, the amplitudes of pressure disturbances along the wall surface for the current case increase before they reach the peak value. However, according to Fig. 5, mode II is predicted by the LST to be always stable. This difference in stability result is not caused by the fact that the effect of the shock is neglected in the LST analysis. A similar numerical simulation study on the stability properties of mode II by using a rectangle domain without the shock shows that the effect from the shock on the mode II stability are negligible.

It is found that the reason for the amplification of wave amplitudes in a stable region of mode II is caused by a resonance between mode II disturbances and the fast acoustic waves outside the boundary layer. From the profiles of mode II disturbances at the inlet shown in Fig. 20, the structure of wave disturbances of mode II does not decay exponentially outside the boundary layer in the synchronization point at the inlet. The mode II wave profiles are very different from those of the same mode at downstream locations (see Fig. 17) where mode II is not synchronized with the fast acoustic wave. In another word, there are strong disturbances outside the boundary layer for mode II near the synchronization point between mode II waves and fast acoustic waves. The disturbances outside the boundary layer belong to fast acoustic waves because the nondimensional amplitudes of disturbances satisfy the dispersive relationship of fast acoustic waves, i.e.,

$$\sqrt{|u'|^2 + |v'|^2} = |p'| M_\infty = \frac{|T'|}{M_\infty (\gamma - 1)} . \qquad (9)$$

Figure 23 compares the nondimensionalized magnitudes of mode II wave at the inlet. The figure shows that the perturbations of mode II outside the boundary layer satisfy the acoustic wave relations given by Eq. (9). In addition, the phase velocities of induced disturbances outside the boundary layer are the same as the phase velocity of a fast acoustic wave, i.e.,

$$a = 1 + M_\infty . \qquad (10)$$

Figure 24 shows the profiles of phase velocities of induced disturbances along the wall-normal direction at different streamwise locations. The phase velocities approach that of a fast acoustic wave in the region outside the boundary layer. The results in both Fig. 24 and Fig. 23 indicate that there are strong acoustic wave components outside the boundary layer in the initial mode II disturbances, which are introduced through the inlet at $x^* = 0.185m$ ($RF = 0.2539$) in the numerical simulation. Figure 24 also shows that the phase velocities of mode II inside the boundary layer decreases as mode II waves propagate to downstream.

Figure 25 shows the comparison of streamwise wave numbers of mode II predicted by the LST and those obtained by the numerical simulations of imposed mode II with the same frequency at different inlet locations. The figure shows that mode II waves are modulated by the fast acoustic wave when mode II are imposed near their initial wave synchronization location. On the other hand, if mode II are imposed at an inlet downstream of the initial point, there is no wave modulation. The wave numbers of the numerical simulation for this case (simulation 1) agree very well with those obtained by the LST.

Figure 26 compares the profiles of disturbances at $x^* = 0.488m$ ($R = 1874.46$ and $RF = 0.4124$) obtained from the numerical simulation with those predicted by the LST. The numerical simulation is for the second case of mode II imposed near the initial wave synchronization location. The figure shows that there is good agreement in the disturbance structures inside the boundary layer between the numerical simulation solutions and eigenfunctions predicted by the LST. However, because a modulation of mode II with the acoustic wave in the simulation, the two sets of results do not agree outside the boundary layer. In the numerical simulation, the wave field downstream contain both mode II wave and a strong acoustic wave components outside the boundary layer. The acoustic wave is excited by mode II through their mutual resonant interaction. It is expected that an imposed forcing acoustic wave can also excite mode II at this synchronization location through their resonant interactions.

Therefore, the characteristics of mode II propagation in the supersonic boundary layer can be summarized as follows. Figure 2 shows that the phase velocities of mode II waves are the same as that of the fast acoustic waves when mode II waves initially appear in the figure. At this initial location, there is a strong resonant interaction between mode II and the fast acoustic waves, because the phase velocities of mode II disturbances are synchronized with that of the acoustic waves. As a result, though predicted to be stable by the LST, mode II disturbances are amplified when they are introduced at the inlet near this synchronization point located at $RF = 0.2539$. Similarly, the amplification of mode I waves is also due to the resonance between

mode I waves and acoustic waves. Since the LST analysis can not account for the interactions between different types of waves, the amplification of mode II disturbances can not be correctly predicted by the LST when there are resonant wave interactions. The current numerical simulation approach based on the full Navier-Stokes equations can take into account for these interactions, as well as the effect of shock interaction with wave modes. On the other hand, when mode II disturbances are introduced through the inlet at a further downstream location with $RF = 0.3552$, the mode II disturbances are mainly confined inside the boundary layer and all disturbances decay exponentially to zero outside the boundary layer (see Fig. 17). In addition, in the downstream after $RF = 0.3552$, the phase velocities of mode II waves are far away from those of the fast acoustic waves as shown in Fig. 25). Therefore, there is no interaction between mode II waves and the acoustic waves in this case. Consequently, there is good agreement on the wave numbers of mode II disturbances between the results from the LST and the numerical simulation, though the LST consistently under predicts the magnitude of the growth rates, due to the effect of non-parallel boundary layer, which is neglected in the LST.

7 Freestream Disturbances

The receptivity of the supersonic boundary layer to freestream disturbance waves are considered by the numerical simulations. The oblique shock plays an important role in the current study because the disturbance waves first pass through the shock before entering the boundary layer. In the simulation, the freestream disturbances are superimposed on the steady base flow to investigate the excitation and the development of boundary-layer instability waves. The effects of the interactions between the oblique shock and freestream disturbances are accurately taken into account by using shock-fitting method. The freestream disturbances are assumed to be weak monochromatic plane acoustic waves before reaching the shock. The perturbations of flow variable in the freestream introduced by the freestream acoustic waves can be written in the following form:

$$\begin{Bmatrix} u' \\ v' \\ p' \\ \rho' \end{Bmatrix}_\infty = \begin{Bmatrix} |u'| \\ |v'| \\ |p'| \\ |\rho'| \end{Bmatrix}_\infty e^{i[k_x x + k_y y - \omega t]}, \quad (11)$$

where $|u'|$, $|v'|$, $|p'|$, and $|\rho'|$ are perturbation amplitudes satisfying the following relations:

$$|u'|_\infty = u_\infty \epsilon k_x/k\,, \qquad |v'|_\infty = u_\infty \epsilon k_y/k\,,$$
$$|p'|_\infty = \rho_\infty C_\infty |u'|\,, \qquad |\rho'|_\infty = |p'|_\infty / C_\infty^2\,,$$

where ϵ is a small nondimensional parameter representing the freestream wave magnitude. The parameter k is the freestream wave number with components k_x and k_y in streamwise and normal direction respectively, i.e.,

$$k_x = k\cos(\theta_{ac}), \qquad k_y = -k\sin(\theta_{ac})\,, \quad (12)$$

where θ_{ac} is the incident angle of the freestream acoustic waves relative to streamwise direction as shown in Fig. 1. The nondimensional wave number is related to the circular frequency ω by dispersion relation:

$$\omega = k\,(\pm c_\infty + u_\infty \cos\theta_{ac})\,, \quad (13)$$

where "$\pm$" are associated with fast or slow acoustic waves respectively. The frequency is characterized by a dimensionless frequency F defined by

$$F = \frac{\omega^* \mu_\infty^*}{\rho_\infty^* u_\infty^{*2}}\,, \quad (14)$$

where ω^* is dimensional circular frequency. The relation between nondimensional circular frequency ω and F is

$$F = \frac{\omega}{R}\,. \quad (15)$$

8 Receptivity to Plane Freestream Fast Acoustic Waves

In this group of cases, plane freestream fast acoustic waves with different frequencies and incident wave angles (θ_{ac}) are imposed at the top of computational boundary in front of the shock. The amplitude of the velocity disturbance in freestream is chosen to be $\epsilon = 5.0 \times 10^{-4}$. The receptivity mechanisms and properties of different boundary-layer discrete normal modes to plane freestream fast acoustic waves with different incident wave angles, frequencies, and different wall boundary conditions are studied in this section.

A plane freestream fast acoustic wave at $F = 2.2 \times 10^{-4}$ with zero angle ($\theta_{ac} = 0$) was studied in our previous paper [15]. However, different components of discrete wave modes involved in boundary-layer disturbances was not completely identified. Therefore, the

same case are studied here in order to completely identify all different wave modes induced in boundary-layer disturbances by forcing freestream fast acoustic waves.

Identification of wave mode

Figure 27 shows the distribution of instantaneous pressure perturbations along the wall surface induced by a plane freestream fast acoustic wave at $F = 2.2 \times 10^{-4}$ with zero angle. Pressure perturbations on the wall shows complex wave patterns, which indicates the existence of a number of wave modes generated in the boundary layer by the receptivity process. According to Mack [6] and Gaponov's [22] study, transmitted acoustic waves can penetrate the boundary layer and form the Stokes waves with continuous spatial spectral as well as discrete wave modes in the boundary layer. Stokes waves are combination of acoustic waves, vorticity waves and entropy waves. Among Stokes waves, the component of acoustic waves is dominant in this case. The discrete wave modes induced in the boundary layer include both Mack modes and a family of stable modes of mode I, mode II, etc. Based on our previous study [15], the second Mack-mode disturbances are expected to be the dominant instability waves in a local region between $x^* = 0.1m$ ($R = 848.5$) and $x^* = 0.2m$ ($R = 1200$). However, this figure shows that there are no dominant second-mode disturbances shown in this range. On the contrary, a clearly dominant wave mode appears after $x^* = 0.2m$. Its amplitudes increase before reaching a peak value at $x^* \approx 0.31m$, although all normal modes are stable in this region predicted by the LST analysis. In fact, a strongly unstable band lying at frequencies above the second-mode one was also observed in Kendall's [21] experiment on hypersonic boundary-layer disturbances induced by acoustic waves. So far, the contradiction on the stability of boundary-layer normal mode between experimental observation and LST prediction has not been resolved yet. Therefore, it is necessary to identify all different wave modes in the boundary layer in order to understand the receptivity mechanisms.

The change of pressure perturbations along the wall surface in the downstream shown in Fig. 27 has a very similar pattern as that of mode II when a single mode II wave is introduced at the inlet with $RF = 0.2539$ shown in Fig. 22. Though mode II is linearly always stable as predicted by LST, it was shown that the growth of mode II is caused by a resonance between mode II disturbances inside the boundary layer and fast acoustic waves outside the boundary layer in the region near the synchronization point between the two waves. Figure 28 compares the amplitudes of pressure perturbations along the wall surface due to two different ways of imposing disturbances: the current case of plane freestream fast acoustic waves and the previous case of imposing mode II wave at the inlet located at $x^* = 0.185m$ (Fig. 22. The amplitude of mode II waves which are introduced at the inlet is multiflied by a factor so that the maximum amplitude of pressure perturbations on the wall surface are the same as that induced by plane freestream fast acoustic waves in current case. This figure shows that the two cases have very similar pattern of growth and decay in pressure perturbations. Hence the receptivity to freestream fast acoustic wave generates mode II waves in this region. To support this conclusion, Fig. 29 compares the profiles of induced disturbances with the structure of mode II wave obtained from LST at $x^* = 0.362m$ ($R = 1614.43$). It shows that the structure of induced disturbances inside the boundary layer ($y/L < 12.9$) matches the structure of mode II wave from LST very well. The differences in the region outside the boundary layer is due to the existence of transmitted acoustic waves outside of the boundary layer. Therefore, the boundary-layer disturbances in the downstream ($x^* > 0.2m$) of current case contain a dominant mode II.

The phase velocities of the induced boundary-layer disturbances are calculated based on pressure perturbations by using temporal Fourier analysis. Figure 30 shows the distribution of the phase velocities along the wall surface. The phase velocities of the first and the second Mack modes, and modes I and II from the LST are also plotted in the same figure for comparison with the numerical solutions. The figure shows that as freestream fast acoustic waves enter the boundary layer, phase velocities of the induced waves is close to those of mode I waves in the upstream region ($x^* < 0.1m$). This indicates that mode I waves are generated inside the boundary layer due to the resonant interaction between mode I waves and fast acoustic waves. near the leading edge. This is confirmed by the fact that the structures of the induced disturbances can match the structure of mode I in this region, which is shown in Fig. 31. Figure 31 compares the structure of disturbances induced by freestream fast acoustic waves and the structure of mode I disturbances from LST at a grid station ($x^* = 0.065m$), After passing the first peak (at $x^* = 0.065m$), mode I waves decay due to its inherent stable properties after its phase velocities decrease and there is no more resonance between mode I waves and acoustic waves. Before mode I waves die out during the propagation, they are synchronized with the Mack mode. As shown in Fig. 4 both the first mode and mode I have almost the same profiles of disturbances across the boundary layer at the synchronization point. As a result, mode I waves convert to the Mack-mode waves in the synchronization region (Fig. 30). Fig. 30 shows a strong oscillation in the region between $x^* = 0.1m$ and $x^* = 0.2m$, where the second

mode is expected to be dominant. The oscillation in the phase velocity curve results from the modulation between the second mode waves and Stokes waves.

In the region of further downstream ($x^* > 0.2m$), Fig. 30 shows that the disturbances in the boundary layer are dominated by a wave mode and the phase velocity of which is close to that of mode II. As shown in Fig. 29, the the structures of induced disturbances match the structure of mode II predicted by LST in this region. If further downstream at location of $x^* > 0.5m$, the mode II waves die down due to their inherent stable properties. As a result, no dominant modes exists in this region. Therefore, there are strong oscillations in phase velocities again in further downstream.

Response coefficient

In the current study, it is found that the Mack-mode waves and fast acoustic waves have very different wave numbers. This fact can be used to extract the wave components of the the second Mack mode from the overall disturbance field in the boundary layer by means of a spatial Fourier analysis. After identification of different discrete modes included in boundary-layer disturbances induced by freestream fast acoustic waves, Fourier analysis and a band-pass filter is used to decompose the second mode waves from the total boundary-layer disturbances. This wave decomposition method has sucessfully been used in our previous study [15].

Response coefficients of the boundary-layer normal modes, such as Mack mode, mode I and mode II, are defined to to quantitatively study the acoustic receptivity of the boundary layer. Specifically, the response coefficient of the boundary layer to forcing disturbances for a given mode in this paper is defined as

$$K_{mode} = \frac{|p'_{mode}|}{|p'_{\infty}|} \tag{16}$$

where $|p'|_{mode}$ is the maximum amplitude of pressure perturbations for the wave mode. For the second mode, this maximum value is located at branch II neutral point of the decomposed second wave fields. Hence, the response coefficient for the second mode is in fact the receptivity coefficient commonly defined in receptivity studies, i.e., the ratio of the decomposed second mode maximum amplitude over the forcing wave amplitude.

In upstream region near the leading edge, the disturbance waves after removing the second mode are dominated by mode I waves. The response coefficient for mode I wave is close to the receptivity coefficient of mode I. In the downstream region, mode II waves are dominant. The response coefficient for mode II wave in this region is close to the receptivity coefficient of mode II. It is should noted that the disturbances in mode I and mode II dominant regions also contain some minor components of the Stokes waves, which cannot be separated from mode I and mode II waves. As discussed earlier, the acoustic wave components are relatively very weak in the peak locations of mode I and mode II waves. Therefore, we use response coefficient instead of receptivity coefficient for mode I and mode II waves. For example, for the current case of freestream fast acoustic waves at zero incident angle, the response coefficients for mode I, the second mode and mode II are:

$$\begin{aligned} &\text{Second mode: } K_{2nd} = 1.03 \\ &\text{Mode I: } K_I = 1.75 \\ &\text{Mode II: } K_{II} = 2.14 \end{aligned}$$

Mode II has much stronger receptivity than the other two mdoes because its resonant interaction with the fast acoustic wave.

Effects of incident angles of the forcing waves

The forcing fast acoustic waves in the freestream can impinge on the flat plate at different incident angles. The effects of incident angles on the receptivity are studied by numerical simulations on receptivities of the Mach 4.5 boundary layer to freestream fast acoustic waves at different incident angles. Specifically, 12 computational cases of different incident wave angles θ_{ac} are considered. The following forcing incident wave angles θ_{ac} have been considered:

#	1	2	3	4	5	6
θ_{ac}	0	7.5	15.0	18.0	20.0	22.5
#	7	8	9	10	11	12
θ_{ac}	30.0	37.5	45.0	60.0	75.0	90.0

All other flow conditions are the same for these cases. Especially, the frequency of different cases are the same at $F = 2.2 \times 10^{-4}$.

In this paper, the receptivity characteristics of second mode, mode I, and mode II are measured by response coefficients defined in Eq. (16). As discussed earlier, the response coefficients calculated in this paper for the second mode, K_{2nd}, are the same as receptivity coefficients defined by most researchers in this field. Figure 33 shows the response coefficients for computational cases of different incident fast acoustic wave angles. Each symbol in the plot represents one of the 12 computational cases of different impinging angles with the same frequency. It shows that the receptivity of the mode II (and mode I to less degree), which is lin-

early stable from LST, has a much stronger receptivity response to the forcing waves than that of the unstable second mode. This figure is a significant because it demonstrates the importance of stable modes in the receptivity process and shows the effects of incident wave angles on the receptivity process.

Figure 33 shows that for a fixed frequency of the current case, there is an "optimal" incident angle θ_{ac} for each wave mode to reach a maximum wave amplification. The maximum receptivity for mode II is reached for incident wave angles in the range between 18° and 22.5°. The maximum receptivity for mode I is reached for θ_{ac} around 45°. On the other hand, the receptivity coefficient for the second mode is less sensitive to the change of the incident wave angles. The maximum receptivity for the second mode is reached for θ_{ac} around 26°. The second mode is not very sensitive to the incident wave angles because the second mode is unstable in this case. The linear growth of the second mode is independent of the forcing waves, which can only affect the initial conditions of the second mode growth.

Effect of wall temperature conditions

In the current study, the steady base flow field is always the same supersonic boundary layer flow over a flat plate with an adiabatic wall boundary condition. For the temperature disturbances in the unsteady solutions, either adiabatic or isothermal conditions can be used for the perturbations only. The temperature perturbation condition in practical applications will be somewhere between these two extreme cases. For this reason, both boundary conditions have been considered in this paper. In this section, the effect of the wall temperature perturbation boundary conditions on the receptivity are compared by numerical simulations.

To study the effect of wall temperature perturbation conditions on the boundary-layer receptivity properties, the receptivity to plane acoustic waves at a fixed $F = 2.2 \times 10^{-4}$ are considered. Both isothermal wall and adiabatic wall boundary conditions are used while all other flow conditions are same. The forcing fast acoustic waves in the freestream can impinge on the flat plate at different incident angles. The effects of incident angles on the receptivity are studied by numerical simulations on receptivities of the Mach 4.5 boundary layer to freestream fast acoustic waves at different incident angles. Adiabatic wall boundary condition is used in all these cases. Specifically, 12 computational cases of different incident wave angles θ_{ac} are considered.

Figure 32 compares the amplitudes of pressure perturbations induced by freestream fast acoustic waves at $\theta_{ac} = 0°$ for the two cases of the different wall boundary conditions for the temperature perturbations. The figure shows a very similar wave patterns for both cases of different wall temperature conditions. The main differences are the fact that the amplitudes of pressure perturbations on the wall for the case of the isothermal wall are smaller than those of the case of the adiabatic wall. A close examination of the peaks of mode I, the second mode, and mode II in the figure shows that the second mode is much weaker for the isothermal case, while mode I and mode II are not affected very much by the change in the wall temperature perturbation conditions. Quantitatively, the response coefficients are calculated for mode I, the second mode and mode II for the isothermal case are

Second mode: $K_{2nd} = 0.187$
Mode I: $K_I = 1.45$
Mode II: $K_{II} = 1.62$

Compared the results for the adiabatic case shown previously, the response coefficients of the second mode in the adiabatic case is 5.5 times as large as that of the isothermal case. On the other hand, the response coefficients of mode I and mode II in the adiabatic case are only 1.2 and 1,3 times as large as those of the isothermal case. Therefore, due to the different receptivity and stability mechanisms between the second mode, and mode I and mode II, the use of isothermal wall boundary condition substantially stabilize the second mode, but does not affect mode I and mode II very much.

Figure 33 compares response coefficients as a function of the incident wave angles for two groups of cases with different wall boundary conditions for the temperature disturbances. The response coefficients distributions are very similar for two groups of cases of different boundary conditions except that the values are smaller for the cases of an isothermal wall. In particular, the response coefficients of the second mode are several times smaller for the cases of an isothermal wall than those for the cases of an adiabatic wall. On the other hand, the response coefficients for mode I and mode II of the isothermal cases are only moderately smaller than those of the adiabatic cases. The incident angle at which mode II reaches maximum response coefficient is also about the same for the two group of wall boundary conditions. The difference in response coefficients for mode I and mode I and for the second mode is again due to their different receptivity mechanisms.

The general trend on the effects of wall temperature perturbation boundary conditions are also true for computational cases of other frequencies. Figure 34 and 35 show the effect of different wall boundary condi-

tions on the amplitudes of pressure perturbations along the wall surface due to plane freestream fast acoustic waves with incident wave angle of $\theta_{ac} = 22.5°$ at two different frequencies: (a) $F = 1.6 \times 10^{-4}$, and (b) $F = 1.2 \times 10^{-4}$. For both frequencies, pressure amplitudes are smaller for the cases of isothermal wall than those for the adiabatic wall. For the case of $F = 1.6 \times 10^{-4}$, the response coefficients of mode I, the second mode and mode II for the isothermal case and the adiabatic case are:

Isothermal Case	**Adiabatic Case**
$K_{2nd} = 0.87$	$K_{2nd} = 5.61$
$K_I = 2.82$	$K_I = 3.47$
$K_{II} = 5.47$	$K_{II} = 7.45$

Again, the response coefficients of modeI and mode II are relative close between the isothermal case and the adiabatic case. However, the response coefficients of the second mode of the adiabatic case is 8.56 times as large as that of the isothermal case. As discussed earlier, for the cases of $F = 1.2 \times 10^{-4}$, mode II waves do not appear in the computational domain because the domain is not long enough. The response coefficients of mode I and the second mode of the isothermal case at this frequency are 3.19 and 2.44 respectively. The corresponding values of adiabatic case are 4.50 and 13.2 for mode I and the second mode, respectively. Again, the response coefficient of the second mode for the adiabatic case is 5.41 times as large as that of the isothermal case at $F = 1.2 \times 10^{-4}$. The reasons for the different response coefficients of the second mode between isothermal case and adiabatic case can be explained from Fig. 14. Specifically, all normal modes are more stable in the isothermal case than the adiabatic case as predicted by the LST (Fig. 7). The second mode waves are converted from mode I waves. Compared with an adiabatic case, mode I in an isothermal case is less amplified before it reaches the first peak in pressure perturbations, which is shown in Fig. 14. Furthermore, the amplitudes of mode I disturbances in the isothermal case decay much faster and die down to a much smaller value when the wave reached the synchronization point between mode I and the Mack mode and converted to the second mode. As a result, the initial amplitude of the induced second mode is much smaller in the isothermal case than that in the corresponding adiabatic case. In addition, the growth rates of the second mode are smaller for the isothermal case than those for the adiabatic case. Therefore, the amplitude of induced second mode at branch II neutral stability point is significantly smaller for the isothermal case than that for the adiabatic case.

The results of the receptivity characteristics of mode I, the second mode and mode II with different wall boundary conditions can explain some discrepancy between the LST predictions and the results of boundary-layer stability experiments. Measurements in the laminar boundary layer on a flat plate by Kendall [21] and Wendt *et al.* [23], and a hollow cylinder by Stetson *et al.* [24] did not show the expected dominance of high-frequency second mode instabilities. In reality, the temperature perturbations on the wall could not follow the adiabatic condition even though the steady flow satisfies a adiabatic condition on the wall. For high frequency disturbances, the temperature perturbations on the wall performs more close to the isothermal wall condition. From our numerical simulation studies of the boundary-layer receptivity with an isothermal wall for perturbations, the induced second mode from mode I is very weak due to the stable property of mode I as discussed in section 6.2. In addition, the subsequent amplification of the second mode disturbances are very weak because the linear stability is much weaker for the isothermal cases. On the other hand, strongly unstable modes in a frequency band, where the second mode is predicted to be stable by LST, were observed in Kendall's experiment on hypersonic boundary-layer disturbances induced by acoustic waves. This can be explained by the amplification of mode I and mode II due to their resonance with the acoustic waves. Again, though they are linearly stable modes, mode I and mode II play an important in the boundary-layer receptivity process.

9 Receptivity to Plane Freestream Slow Acoustic Waves

In this group of cases, plane freestream slow acoustic waves with different frequencies and incident wave angles (θ_{ac}) are imposed at the top of computational boundary in front of the shock. Isothermal wall boundary condition is used for temperature perturbations on the wall in this group of cases. The amplitude of the velocity disturbance in freestream is chosen to be $\epsilon = 5.0 \times 10^{-4}$. There receptivity of boundary layer to a plane freestream slow acoustic wave at $F = 1.6 \times 10^{-4}$ with zero incident angle are analyzed first. The effect of incident wave angle of freestream slow acoustic wave on the receptivity are studied in the next step.

Slow acoustic wave ($F = 1.6 \times 10^{-4}$ and $\theta_{ac} = 0°$)

Figure 36 shows the contours of instantaneous pressure perturbations induced by a plane freestream slow acoustic wave at $F = 1.6 \times 10^{-4}$ with zero incident angle. There are strong transmitted slow acoustic waves

propagating in the direction almost parallel to the wall surface. Meanwhile, strong boundary-layer disturbances are induced by forcing slow acoustic waves. Figure 37 also shows the local pattern of density perturbations in the region ($0.2m < x^* < 0.35m$), where the second mode is expected to be dominant based on the discussion in section 6.1. Unlike boundary-layer disturbances induced by forcing fast acoustic wave, there are clear rope-like second-mode disturbances shown in boundary-layer disturbances induced by forcing slow acoustic waves.

Figure 38 shows the distribution of instantaneous pressure perturbations along the wall surface. The change of amplitudes in pressure perturbations has a very similar pattern as that of the second mode when a single second mode at $F = 1.6 \times 10^{-4}$ is introduced at the inlet $x^* = 0.025m$. In addition, the induced wave structure profiles in the region ($0.2m < x^* < 0.35m$) can match those of the second mode obtained from LST. Therefore, the boundary-layer disturbances induced by forcing slow acoustic waves are dominated by the second mode waves. The induced second mode waves grow before reaching the Branch II neutral stability point due to their unstable property. As discussed in section 6.1, the locations of branch II neutral stability point of the second mode in terms of $R * F$ are same for different frequencies. For isothermal case, the second-mode branch II neutral point is located at $RF = 0.2246$ based on the growth rate curve shown in Fig. 7, which is at $x^* = 0.2738m$ for the case of $F = 1.6 \times 10^{-4}$. For the current simulation, the maximum amplitude of pressure perturbations on the wall is located at $x^* = 0.2754m$, which is very close to that from LST prediction.

Figure 39 shows the distribution of the phase velocities based on pressure perturbations on the wall. The phase velocities of the first and the second Mack modes, and modes I and II from the LST are also plotted in the same figure for comparison with the numerical solutions. The phase velocity curve in current case is totally different from the case in which boundary-layer disturbances are induced by freestream fast acoustic waves. First of all, there are neither mode I nor mode II waves shown in the current case. The phase velocity curve in current case can match that of Mack modes, which indicates Mack-mode waves are dominant. This can be easily explained from phase velocity curves of different boundary-layer normal modes shown in 39. After freestream slow acoustic waves enter the boundary layer, the first Mack-mode waves are generated because the synchronization of wave numbers or wave speeds between the first Mack-mode waves and slow acoustic waves near the leading edge. The Mack-mode waves are significantly amplified and become dominant mode waves after enter the second-mode unstable region. After passing the branch II neutral point, the Mack-mode waves die down and becomes no longer dominant due to their stable property. As a result, there are strong oscillations in phase velocity curve in downstream $x^* > 0.4m$.

Effect of incident wave angles

The effects of incident angles on the receptivity are studied by numerical simulations on receptivities of the Mach 4.5 boundary layer to plane freestream slow acoustic waves at $F = 1.6 \times 10^{-4}$ with at 4 different incident angles, i.e., $\theta_{ac} = 0, 22.5, 45$ and 67.5.

Figure 40 shows the wave amplitudes of pressure disturbances on the wall surface due to freestream slow acoustic waves for four different incident wave angles. The dominant Mack-mode waves are induced in all four cases. With increasing incident wave angles, the peak amplitude of induced second Mack-mode waves decrease dramatically. In fact, for different incident angle θ_{ac} of forcing slow acoustic waves, there always exists the component of slow acoustic waves propagating in the direction parallel to the wall surface due to diffraction and diffusion of transmitted slow acoustic waves near the leading edge. However, the amplitude of the component for fast acoustic waves propagating in the direction parallel to the wall surface change significantly with different incident angle θ_{ac}. Specifically, the wave component of slow acoustic waves propagating in the direction parallel to the wall surface decrease as the incident angle θ_{ac} increases. As a result, the initial amplitude of induced first Mack-mode waves decrease as the incident angle increases. The maximum initial amplitude of induced first Mack-mode waves is reached at $\theta_{ac} = 0°$. Due to the different initial amplitudes of first Mack-mode waves induced by slow acoustic waves with different incident angles, the receptivity of unstable second mode is very sensitive to incident slow acoustic wave angles. Figure 41 shows the receptivity coefficients of the second mode as a function of the incident wave angles. The receptivity coefficients of the second mode decrease linearly with increasing incident wave angles.

Slow acoustic wave *vs.* fast acoustic wave

The receptivity of boundary layer to freestream slow acoustic waves are compared with that that to freestream fast acoustic waves in this section. Two cases of receptivity to plane freestream acoustic waves at $F = 2.2 \times 10^{-4}$ with zero incident angle are considered here. One is for plane fast acoustic waves. The other is for slow acoustic waves. Isothermal wall boundary condition is used for temperature perturba-

tions on the wall in both cases. The case of receptivity to fast acoustic waves has been discussed in section 8. The receptivity to a plane slow acoustic wave at $F = 2.2 \times 10^{-4}$ with zero incident angle is studied here. Figure 42 compares amplitudes of pressure perturbations on the wall induced by freestream fast acoustic waves and slow acoustic waves separatedly. While both unstable Mack modes and a family of stable modes, i.e. mode I, mode II, are generated by forcing fast acoustic waves, only Mack modes are excited by forcing slow acoustic waves. Compared with the maximum amplitude of the second mode induced by fast acoustic waves, the peak amplitude of the second mode induced by slow acoustic waves are much larger. Quantitatively, the receptivity coefficient of the second mode by slow acoustic waves shown in Fig. 42 is 0.7013, which is 3.75 times of the receptivity coefficient of the second mode by fast acousic waves ($K_{2nd} \doteq 0.187$) in Fig. 42. Therefore, for the second-mode receptivity to freestream acoustic waves at zero incident angle, slow acoustic waves are more efficient to generate unstable boundary-layer disturbances than fast acoustic waves.

10 Conclusions

In this paper, the receptivity of the supersonic boundary layer to acoustic waves coming from the freestream are studied by numerical simulation.

A LST-code based on multi-domain spectral method has been developed to identify different boundary-layer normal modes. The performances of different boundary-layer normal modes have been studied by both numerical simulation and LST. The results from both DNS and LST show that the phase velocities of normal modes are implicit functions of the product of frequency and Reynolds number ($R * F$). Almost same locations of branch I or II neutral points of second mode in terms of $R * F$ are obtained for different frequencies and Reynolds number. LST results show that all normal modes are stable except that the subsonic mode is unstable in certain small range of $R * F$. The numerical study on the performance of mode I and mode II shows that there are strong resonance between them and acoustic waves, which lead to the amplification of mode I and mode II, although LST results show that both of them are stable. Both mode I and mode-II can get synchronized with the subsonic mode. Different modes have the same structure at the synchronization point. Therefore, it is impossible to distinguish different modes from their structure alone. Mode I can convert to the second mode after they get synchronized with each other.

The receptivity mechanisms for flow over a flat plat at Mach 4.5 to freestream acoustic waves has been studied. All components of boundary layer disturbances induced by free-stream disturbances are identified by comparing with LST. It is found that the forcing fast acoustic waves do not interact directly with the unstable Mack modes. Instead, the stable modes of mode I and mode II play an important role in the receptivity process because they interact with both the forcing acoustic waves and the unstable Mack modes. Through the interactions, the stable modes transfer the wave energy from the forcing freestream fast acoustic waves to the second Mack-mode waves. The effects of incident wave angles, forcing wave frequencies, and wall temperature perturbation conditions on the receptivity are studied. The maximum receptivities of the second mode, mode I and mode II to plane freestream fast acoustic waves are obtained when incident wave angles approximately equal 26°, 45°, and 20°, respectively. The receptivity mechanisms of the second mode are very different from those of mode I and mode II, which lead to very different receptivity properties for these discrete wave modes to freestream fast acoustic waves with different incident wave angles, frequencies, and different wall boundary conditions.

The receptivity mechanisms of the second mode to freestream slow acoustic waves are different from those by freestream fast acoustic waves. Unlike forcing fast acoustic waves, the forcing slow acoustic waves can directly generate Mack-mode waves without exchanging energy with stable boundary-layer normal modes, such as mode I and mode II. For the second-mode receptivity to freestream acoustic waves at zero incident angle, slow acoustic waves are more efficient to generate unstable boundary-layer disturbances than fast acoustic waves.

11 Acknowledgements

This research was supported by the Air Force Office of Scientific Research, USAF, under AFOSR Grand # F49620-00-1-0101. The program manager is Dr. John Schmisseur. The views and conclusions contained herein are those of the author and should not be interpreted as necessarily representing the official policies or endorsements either expressed or implied, of the Air Force Office of Scientific Research or the U.S. Government.

References

[1] M. E. Goldstein and L. S. Hultgren. Boundary-Layer Receptivity to Long-Wave Free-Stream Dis-

turbances. *Annual Review of Fluid Mechanics*, Vol. 21, pp. 137-166 1989.

[2] L. M. Mack. Boundary layer linear stability theory. In *AGARD report, No. 709*, 1984.

[3] A. A. Maslov and N. V. Seminov. Exitation of nature oscillations in a boundary layer. *Fluid Dynamics (Translated From Russian)*, (3):74–78, 1986.

[4] A. A. Sidorenko A. A. Maslov, A. N. Shiplyuk and Arnal D. Leading Edge Receptivity of the Hypersonic Boundary Layer to 3-D Acoustic Waves. *Ineternational Conference on the Methods of Aerophysical Research (ICMAR' 98), Novosibirsk, Russia*, 1998.

[5] A. D. Kosinov N. V. Seminov and A. A. Maslov. An Experimental Study of Instability Disturbances Excitation by External Source in Supersonic Boundary Layer of a Blunted Plate. *Ineternational Conference on the Methods of Aerophysical Research (ICMAR' 98), Novosibirsk, Russia*, 1998.

[6] L. M. Mack. Linear Stability Theory and the Problem of Supersonic Boundary-Layer Transition. *AIAA Journal*, Vol. 13, No. 3, pp. 278-289, 1975.

[7] M. Choudhari and C. L. Strett. Boundary Layer Receptivity Phenomena in Three-Dimensional and High-Speed Boundary Layers. *AIAA paper 90-5258*, 1990.

[8] E. J. Kerschen. Boundary-Layer Receptivity. *AIAA paper 89-1109*, 1989.

[9] A. V. Fedorov and A. P. Khokhlov. Excitation of unstable modes in a supersonic boundary layer by acoustic waves. *Fluid Dynamics (Translated From Russian)*, (4):67–74, 1991.

[10] A. V. Fedorov and A.P. Khokhlov. Perhistory of Instability in a Hypersonic Boundary layer. *Theoretical and Computational Fluid Dynamics*, Vol. 14, pp. 359–375, 2001.

[11] A. V. Fedorov and A. Tumin. Initial-Value Problem for Hypersonic boundary Layer Flows . *AIAA paper 2001-2780*, 2001.

[12] X. Zhong. Direct Numerical Simulation of Hypersonic Boundary-Layer Transition Over Blunt Leading Edges, Part II: Receptivity to Sound . *AIAA paper 97-0756, 35th AIAA Aerospace Sciences Meeting and Exhibit, January 6-9, Reno, Nevada*, 1997.

[13] X. Zhong. Leading-edge receptivity to freestream disturbance waves for hypersonic flow over a parabola. *Journal of Fluid Mechanics*, 441:315–367, 2001.

[14] R. Lin M. R. Malik and R. Sengupta. Computation of Hypersonic Boundary-Layer Response to External Disturbances. *AIAA paper 99-0411*, 1999.

[15] Y. Ma and X. Zhong. Numerical simulation of receptivity and stability of nonequilibrium reacting hypersonic boundary layers. AIAA Paper 2001-0892, AIAA, 2001.

[16] X. Zhong. High-Order Finite-Difference Schemes for Numerical Simulation of Hypersonic Boundary-Layer Transition. *Journal of Computational Physics*, 144:662–709, 1998.

[17] M. R. Malik. Stability theory for chemically reacting flows. In D. Arnal and R. Michel, editors, *Laminar-Turbulent Transition, IUTAM Symp., Toulouse, Springer-Verlag*, 1990.

[18] J. M. Kendall. Supersonic boundary layer stability experiments. *Proceedings of Transition Study Group Meeting, edited by W. D. McCauley*, 2(A), 1965. Aerospace Corp., San Bernardino.

[19] C. D. Pruett and C. L. Chang. A Comparison of PSE and DNS for High-Speed Boundary-Layer Flows. *Transitional and Turbulent Compressible Flows*, L. D. Kral and T. A. Zang, editors, pp. 57-67, FED-Vol. 151, ASME, 1993.

[20] L. Kleiser Y. Guo and N. A. Adams. Comparison of temporal and spatial direct numerical simulation of compressible boundary-layer transition. *AIAA Journal*, 34(4):683–690, 1996.

[21] J. M. Kendall. Wind Tunnel Experiments Relating to Supersonic and Hypersonic Boundary-Layer Transition. *AIAA Journal*, Vol. 13, No. 3, pp. 290–299, 1975.

[22] S. A. Gaponov. Interaction of supersonic boundary layer with acoustic disturbances. *Fluid Dynamics (Translated From Russian)*, (6):51–56, 1977.

[23] V. Wendt and M. Simen. An experimental and theoretical investigation of instabilities in hypersonic flat plate boundary layer flow. *Physics of Fluids*, Vol. 7, No. 4, pp. 877-887, 1995.

[24] K. F. Stetson, E. R. Thompson, J. C. Donaldson, and L. G. Siler. A comparison of planar and conical boundary layer stability and transition at a Mach number of 8. *AIAA paper 91-1639*, 1991.

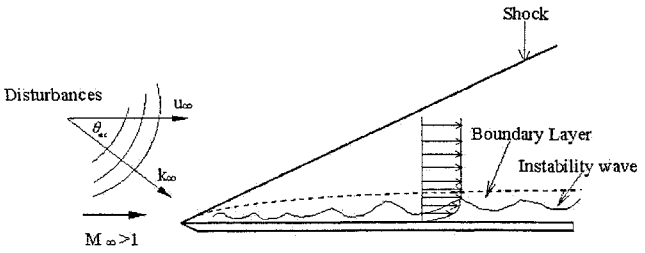

Figure 1: A schematic of the receptivity to freestream disturbances for a supersonic boundary layer over a flat plate.

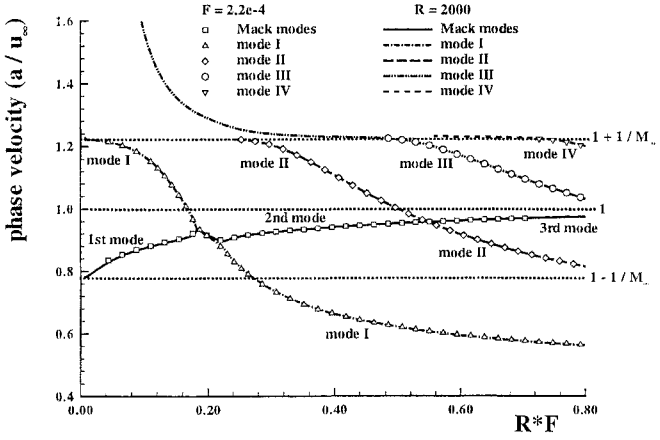

Figure 2: The distribution of the phase velocities of boundary-layer waves modes as a function of RF obtained by the LST, either at different R with a fixed $F = 2.2 \times 10^{-4}$ or at different F with a fixed location at $R = 2000$ ($M_\infty = 4.5$ and $Re^*_\infty = 7.2 \times 10^6/m$).

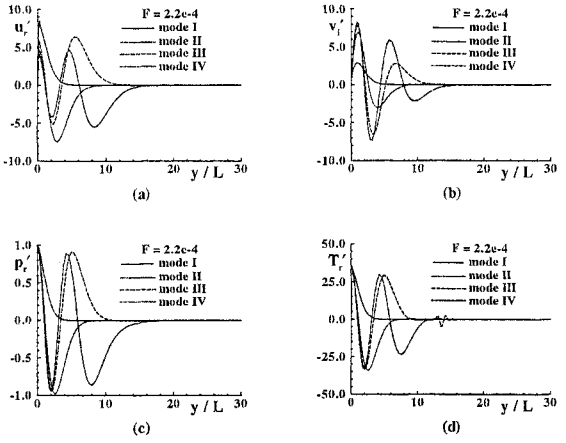

Figure 3: Profiles of stable boundary-layer normal modes (mode I, mode II, etc) obtained by the LST at R = 4000 ($F = 2.2 \times 10^{-4}$).

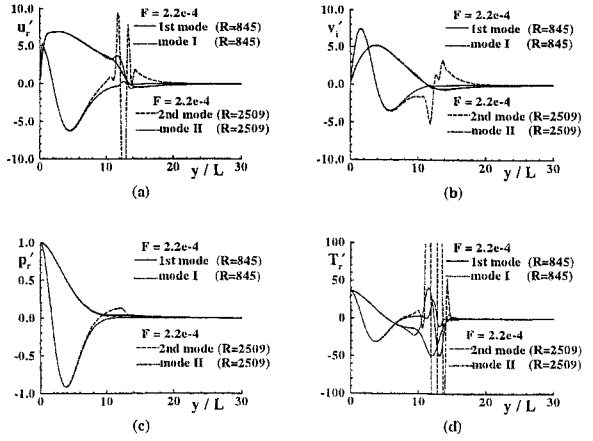

Figure 4: Comparison of profiles of mode I and mode II with the Mack modes (first and second modes) at the locations of wave synchronization points.

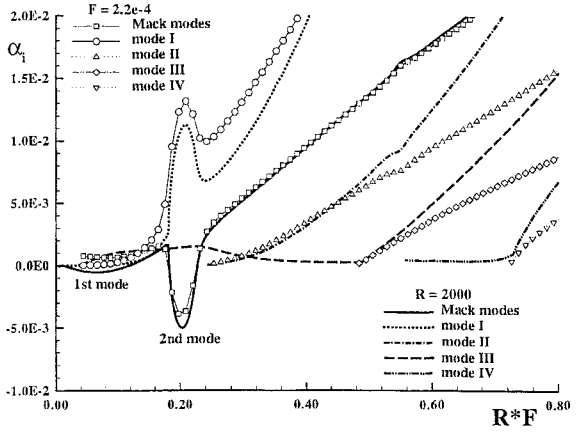

Figure 5: The distribution of the growth rates of boundary-layer waves modes as a function of RF obtained by the LST.

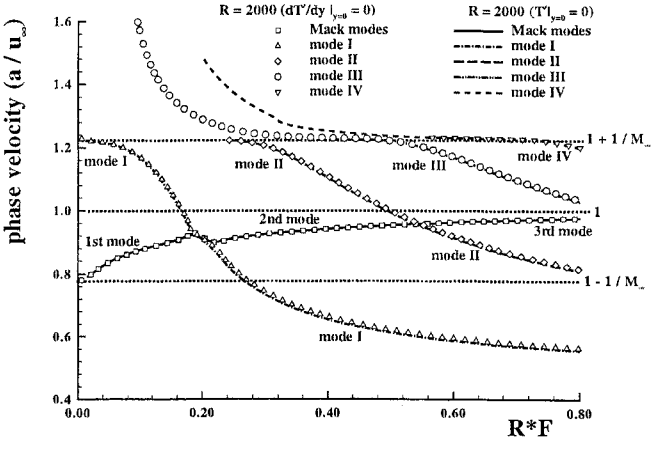

Figure 6: Comparison of phase velocities of boundary-layer normal modes between the isothermal case and the adiabatic case.

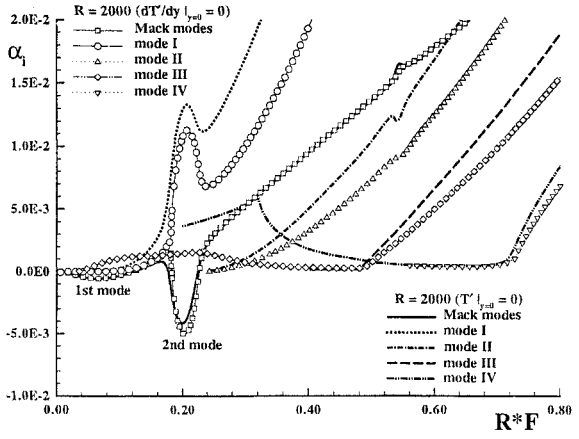

Figure 7: Comparison of growth rates of boundary-layer normal modes between the isothermal case and the adiabatic case.

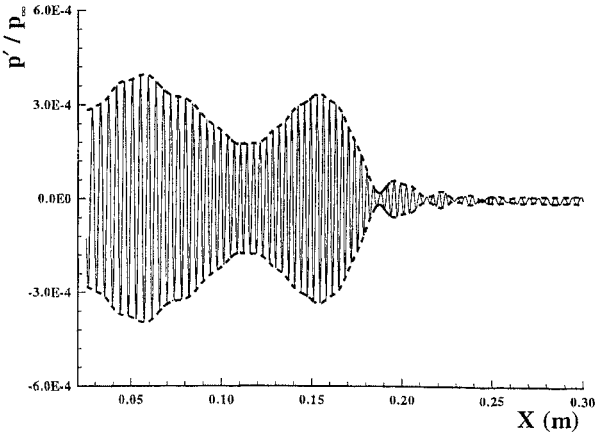

Figure 10: Distribution of instantaneous pressure perturbations along the wall surface ($F = 2.2 \times 10^{-4}$).

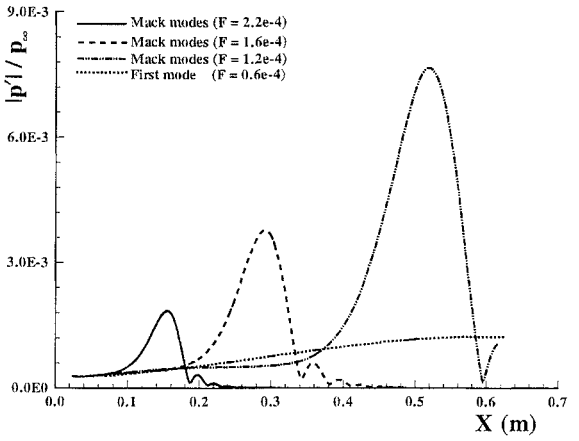

Figure 8: Distribution of amplitudes of pressure perturbations of the Mack mode at different frequencies.

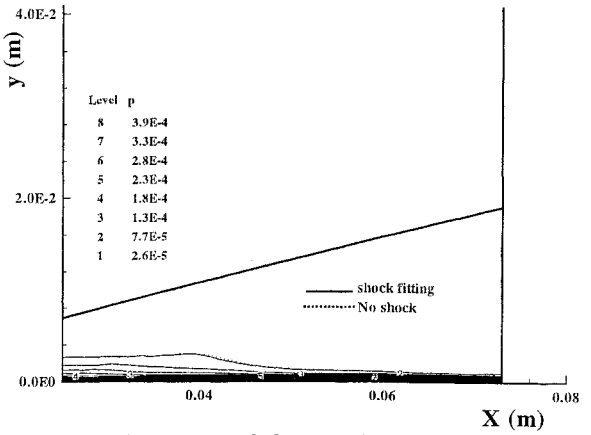

Figure 11: Contours of the amplitudes of pressure disturbances for the case of imposed mode I at the inlet ($F = 2.2 \times 10^{-4}$).

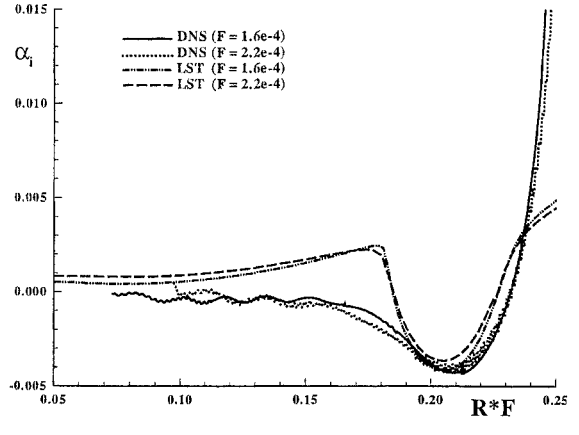

Figure 9: Comparison of the growth rates of the Mack mode between the LST and simulation results for two sets of frequencies: $F = 2.2 \times 10^{-4}$ and $F = 1.6 \times 10^{-4}$.

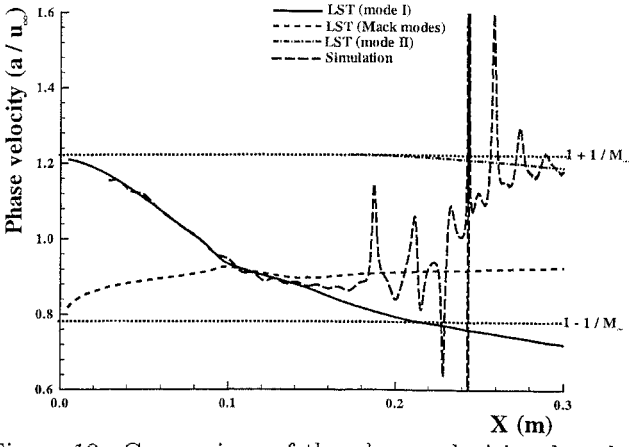

Figure 12: Comparison of the phase velocities, based on pressure disturbances on the wall, of the numerical solutions and the LST predictions ($F = 2.2 \times 10^{-4}$).

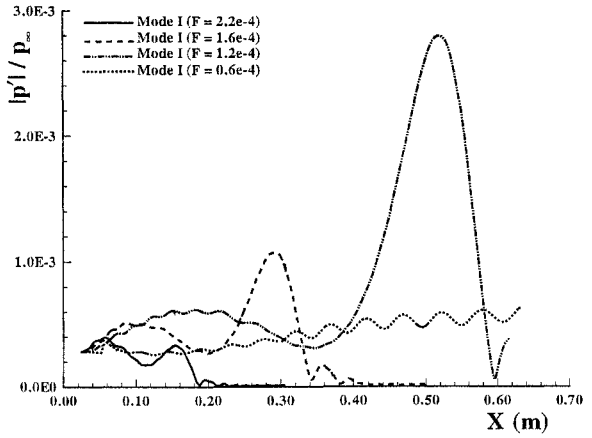

Figure 13: Distributions of the amplitudes of pressure perturbations on the wall for the cases of imposed mode I of different frequencies at the inlet.

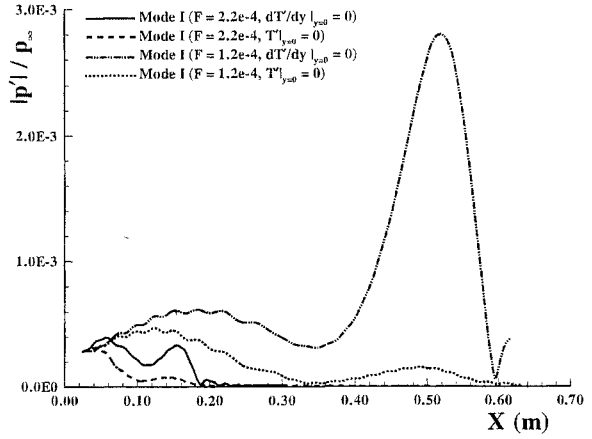

Figure 14: Comparison of the amplitudes of pressure perturbations along the wall surface for mode I with different wall boundary conditions at different frequencies.

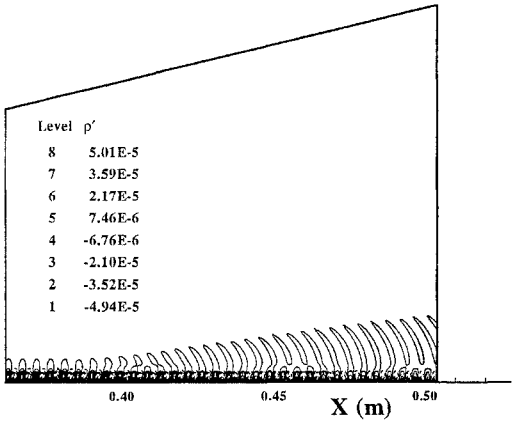

Figure 15: Instantaneous density perturbation contours for the case of imposed mode II at inlet with $RF = 0.3552$ ($F = 2.2 \times 10^{-4}$).

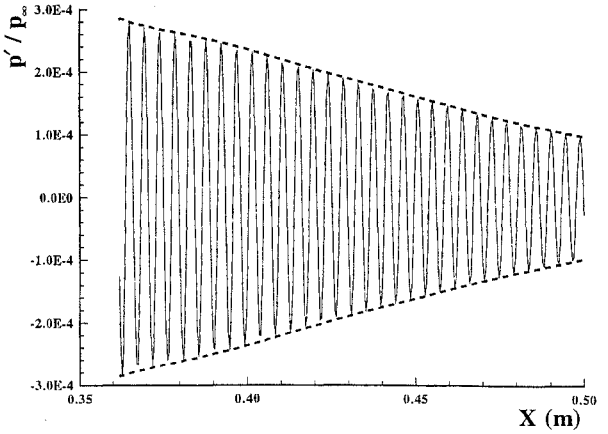

Figure 16: Distribution of instantaneous pressure perturbations of mode II propagation along the wall surface for the case of imposed mode II at inlet with $RF = 0.3552$ ($F = 2.2 \times 10^{-4}$).

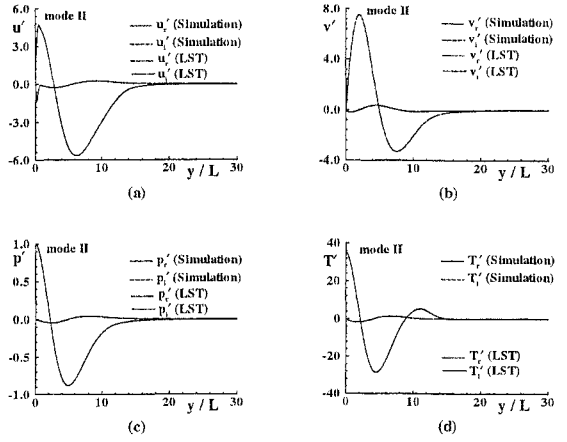

Figure 17: Comparison of the wave structure of mode II obtained by the LST and by numerical simulation for grid station located at $R = 1874.46$ for the case of imposed mode II at inlet with $RF = 0.3552$ ($F = 2.2 \times 10^{-4}$)

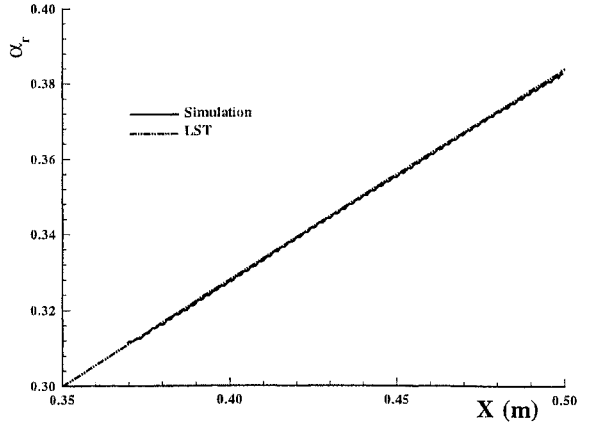

Figure 18: Comparison of the wave number distributions of mode II between the simulation and the LST results for the case of imposed mode II at inlet with $RF = 0.3552$ ($F = 2.2 \times 10^{-4}$).

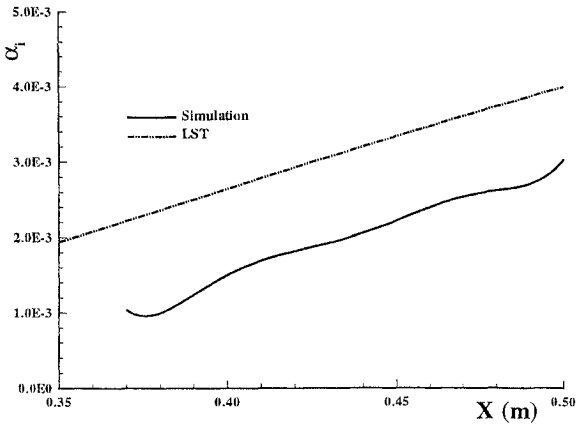

Figure 19: Comparison of growth rate distributions of mode II between the simulation and the LST results for the case of imposed mode II at inlet with $RF = 0.3552$ ($F = 2.2 \times 10^{-4}$).

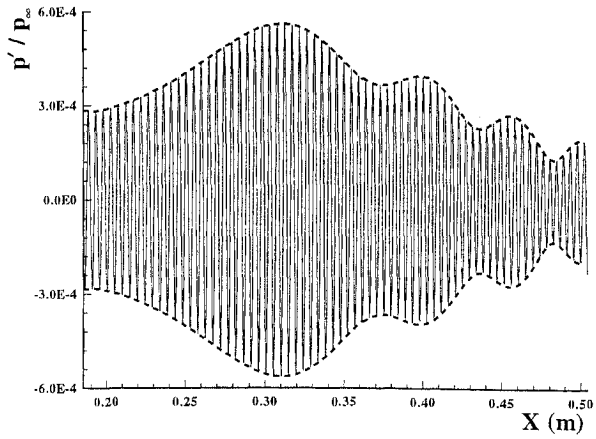

Figure 22: Distribution of instantaneous pressure perturbations of mode II along the wall surface for the case of imposed mode II at the inlet with $RF = 0.2539$ ($F = 2.2 \times 10^{-4}$).

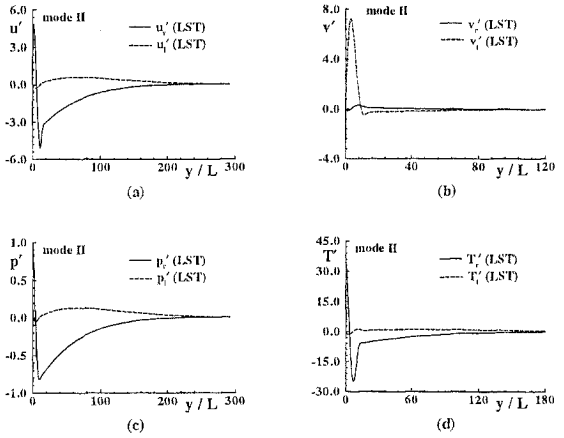

Figure 20: Profiles of mode II disturbances obtained from LST at the inlet located with $RF = 0.2539$ ($F = 2.2 \times 10^{-4}$).

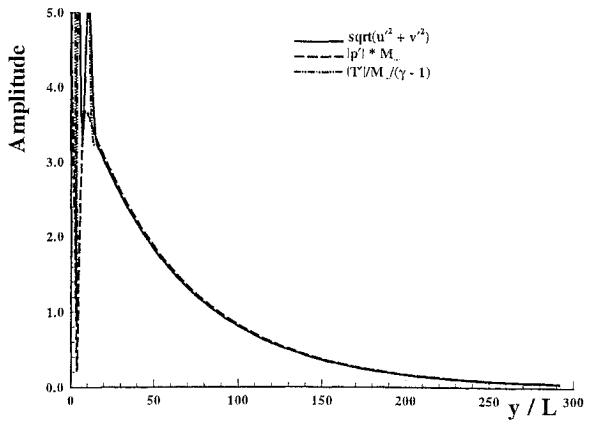

Figure 23: Wave structure of disturbances, obtained from LST, imposed at the inlet with $RF = 0.2539$ ($F = 2.2 \times 10^{-4}$).

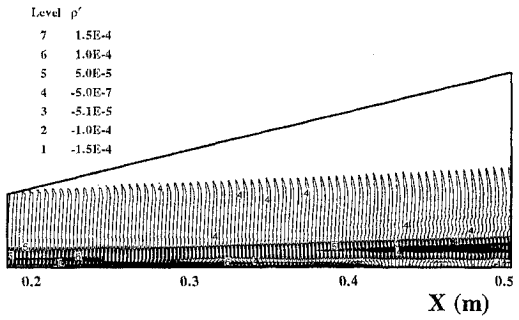

Figure 21: Instantaneous density perturbation contours of mode II propagation in the boundary layer for the case of imposed mode II at the inlet with $RF = 0.2539$ ($F = 2.2 \times 10^{-4}$).

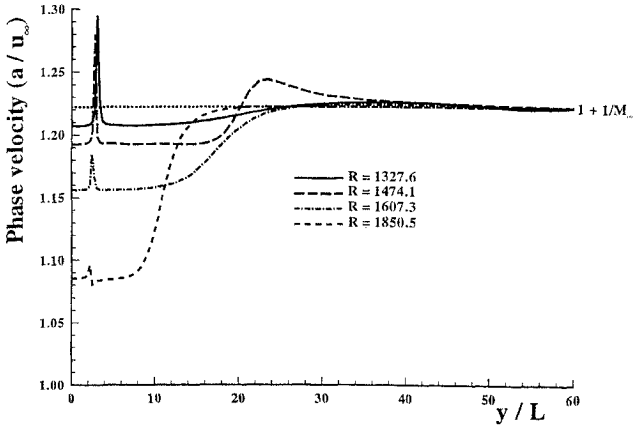

Figure 24: Profiles of phase velocities of wave disturbances obtained by numerical simulations for the case of imposed mode II at the inlet with $RF = 0.2539$ ($F = 2.2 \times 10^{-4}$).

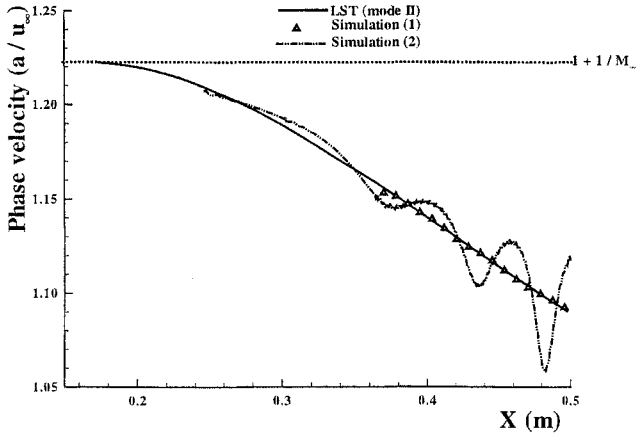

Figure 25: Comparison of phase velocities of the LST and those of numerical simulation mode II disturbances introduced at different locations of inlet (Simulation 1: $R_{inlet} = 1614.43$, simulation 2: $R_{inlet} = 1154.12$, $F = 2.2 \times 10^{-4}$).

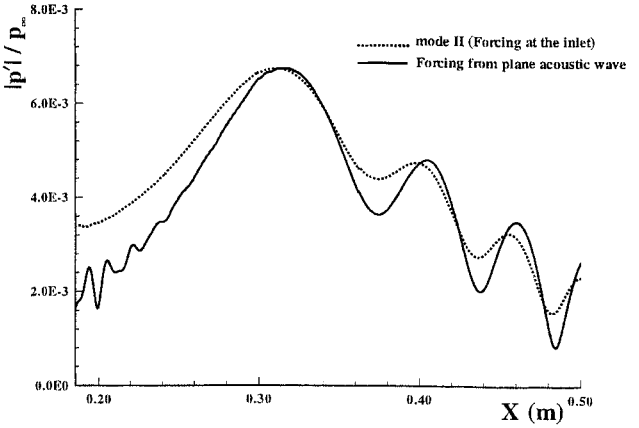

Figure 28: Comparison of amplitudes of pressure perturbations along the wall surface for two cases of different ways of imposing forcing perturbations ($F = 2.2 \times 10^{-4}$).

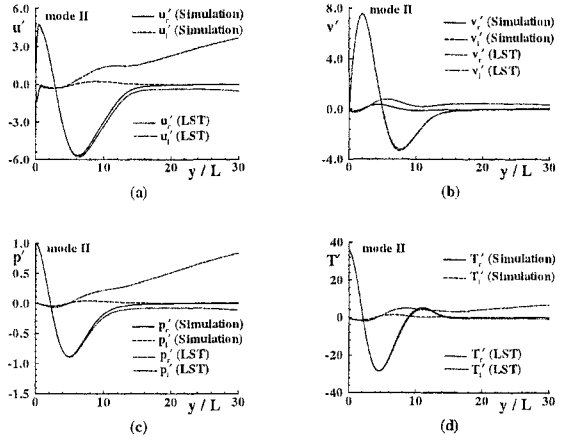

Figure 26: Comparison of the wave structures of mode II between the LST results and the simulation solutions at $R = 1874.46$ ($F = 2.2 \times 10^{-4}$).

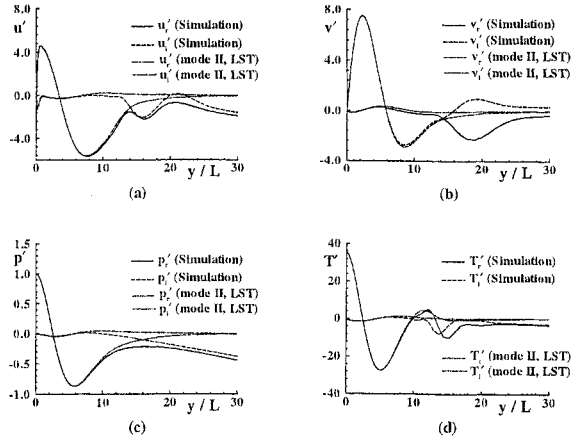

Figure 29: Comparison of the wave structures of disturbances induced by freestream fast acoustic waves and those of mode II obtained by the LST at $R = 1614.43$ ($F = 2.2 \times 10^{-4}$ and $\theta_{ac} = 0°$).

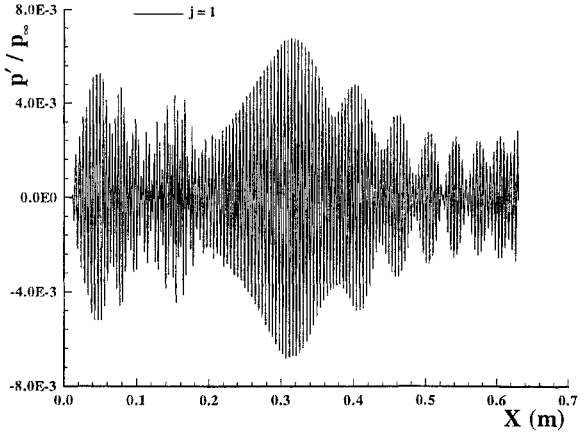

Figure 27: Instantaneous pressure perturbations along the wall surface for the case of a plane acoustic forcing wave from the freestream ($F = 2.2 \times 10^{-4}$ and $\theta_{ac} = 0°$).

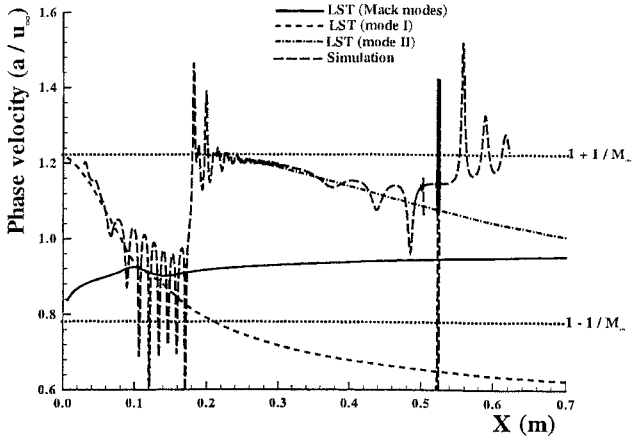

Figure 30: Distribution of phase velocity along the wall surface ($F = 2.2 \times 10^{-4}$ and $\theta_{ac} = 0°$).

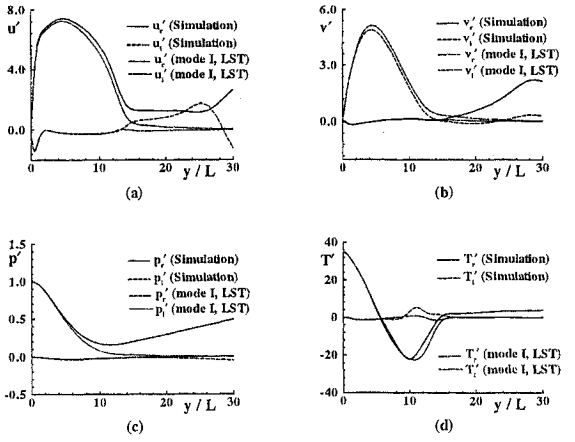

Figure 31: Comparison of the wave structures of disturbances induced by freestream fast acoustic waves and those of mode I disturbances of LST at $R = 684.11$ ($F = 2.2 \times 10^{-4}$ and $\theta_{ac} = 0°$).

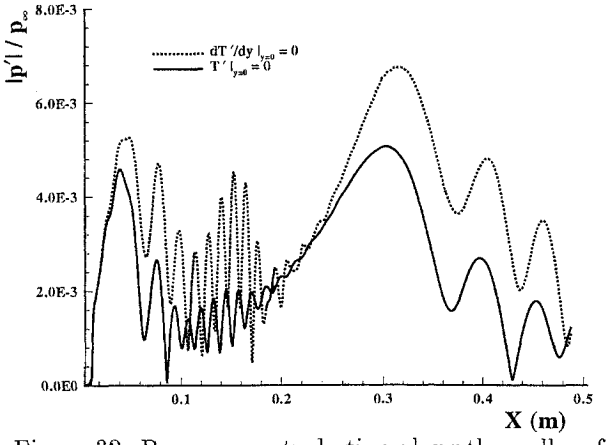

Figure 32: Pressure perturbation along the wall surface induced by freestream fast acoustic waves of zero incident wave angle and different temperature boundary conditions ($F = 2.2 \times 10^{-4}$ and $\theta_{ac} = 0°$).

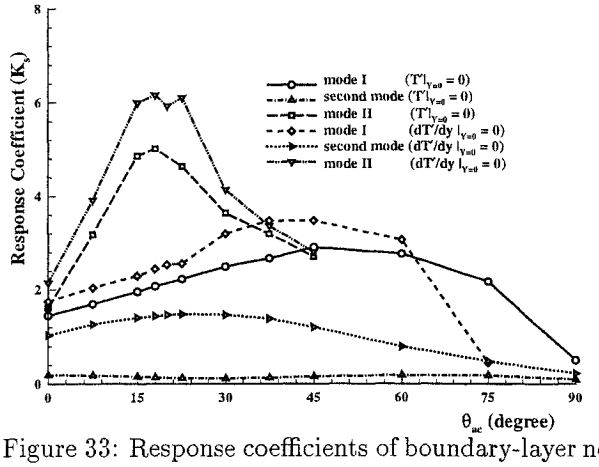

Figure 33: Response coefficients of boundary-layer normal modes to freestream acoustic waves with different wall boundary conditons vs. incident wave angles ($F = 2.2 \times 10^{-4}$).

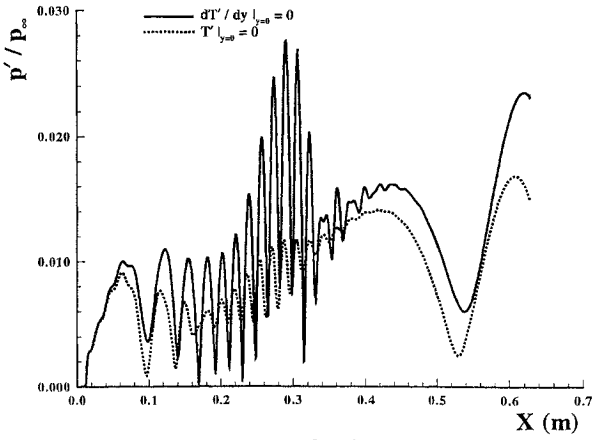

Figure 34: Pressure perturbation amplitudes along the wall surface induced by plane acoustic waves of different boundary conditions ($F = 1.6 \times 10^{-4}$, $\theta_{ac} = 22.5°$).

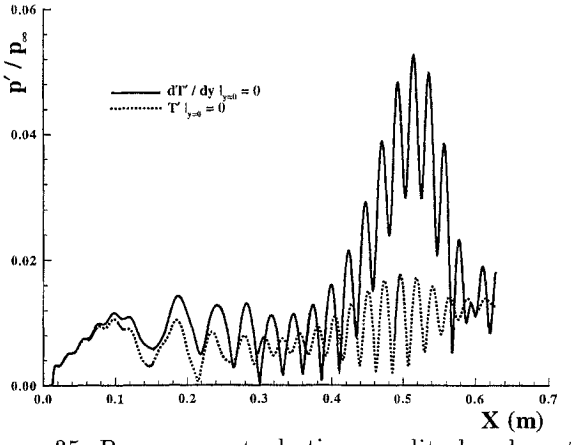

Figure 35: Pressure perturbation amplitudes along the wall surface induced by plane acoustic waves of different boundary conditions ($F = 1.2 \times 10^{-4}$, $\theta_{ac} = 22.5°$).

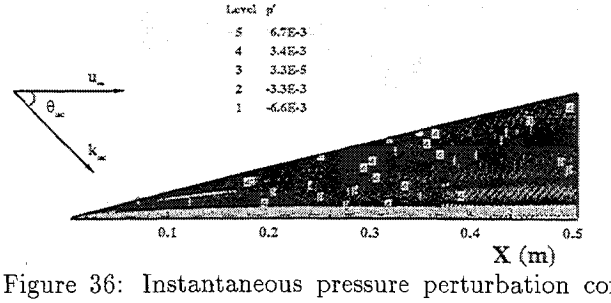

Figure 36: Instantaneous pressure perturbation contours induced by a plane freestream slow acoustic wave ($F = 1.6 \times 10^{-4}$, $\theta_{ac} = 0°$).

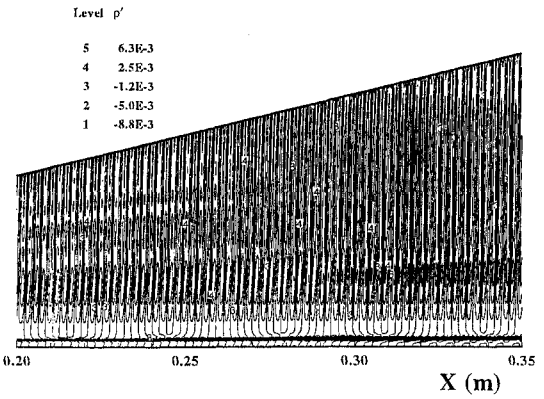

Figure 37: Instantaneous density perturbation contours induced by a plane freestream slow acoustic wave ($F = 1.6 \times 10^{-4}$, $\theta_{ac} = 0°$).

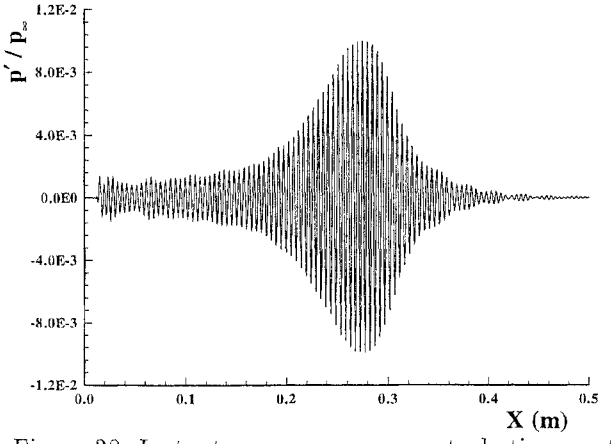

Figure 38: Instantaneous pressure perturbations on the wall induced by a plane freestream slow acoustic wave ($F = 1.6 \times 10^{-4}$, $\theta_{ac} = 0°$).

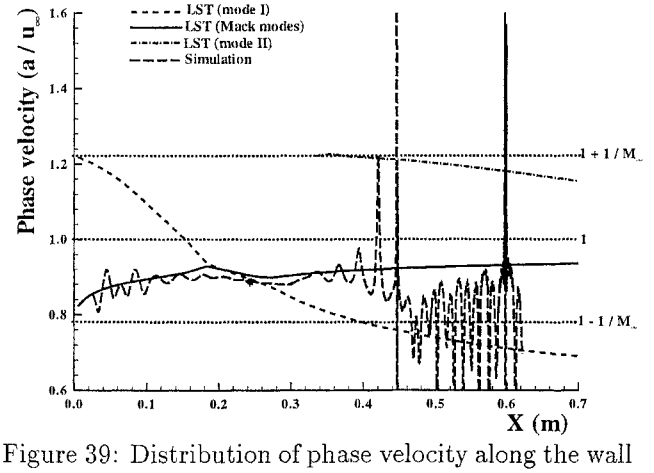

Figure 39: Distribution of phase velocity along the wall surface for boundary-layer disturbances induced by a plane freestream slow acoustic wave ($F = 1.6 \times 10^{-4}$, $\theta_{ac} = 0°$).

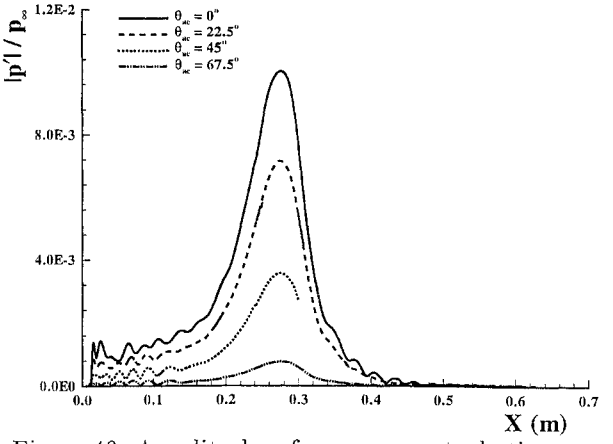

Figure 40: Amplitudes of pressure perturbations on the wall for the cases of freestream slow acoustic waves at different incident wave angles ($F = 1.6 \times 10^{-4}$)

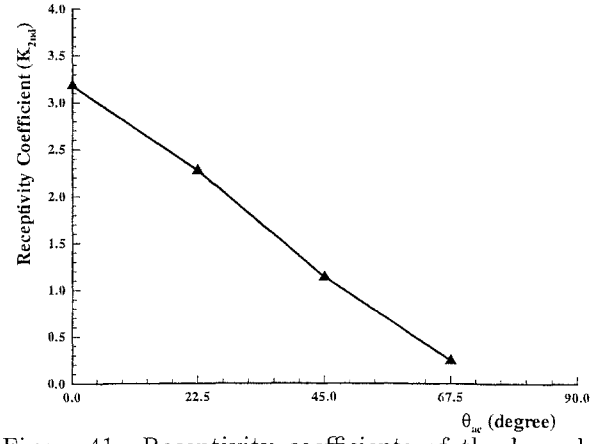

Figure 41: Receptivity coefficients of the boundary-layer second modes to freestream slow acoustic waves vs. incident wave angles ($F = 1.6 \times 10^{-4}$)

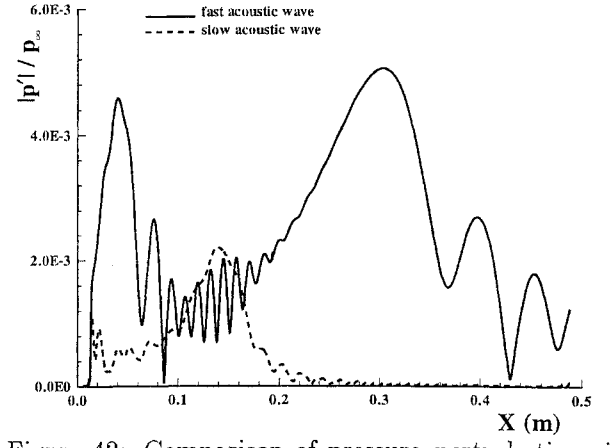

Figure 42: Comparison of pressure perturbations induced by freestream fast acoustic waves vs. that by slow acoustic waves. ($F = 2.2 \times 10^{-4}$ and $\theta_{ac} = 0°$)